

Topic 4.1

STRUCTURE AND STRUCTURE CHANGE PROCESSES

Rapporteur: Robert Hart
Department of Earth, Ocean, and Atmospheric Science
Florida State University
Tallahassee, FL
USA
Email: rhart@fsu.edu
Phone: +1+850+645 1552

Working group (WG) Members listed alphabetically by last name: Sergio Abarca (Naval Postgraduate School), Michael Bell (University of Hawaii), Daniel Chavas (Princeton University), Joshua Cossuth (Naval Research Laboratory), Robert Hart (Florida State University), Andrew Hazelton (Florida State University), Yi-Hsuan Huang (National Taiwan University), Ying Li (Chinese Academy of Meteorological Science), Yumin Moon (University of Oklahoma), Y. V. Rama Rao (India Meteorological Department), Masahiro Sawada (MRI/Japan Meteorological Agency), Daniel Stern (National Center for Atmospheric Research), Diana Stovern (University of Arizona), Jonathan Vigh (National Center for Atmospheric Research)

Abstract: This report summarizes the current state of research on tropical cyclone (TC) structure, structure change and the processes associated with those changes. It is not intended to be an exhaustive summary of all knowledge on the subject, but instead a focus on the developments in this area since the last IWTC (IWTC-VII) in La Reunion in 2010. This report is broken down by sub-subject, generally starting with the inner core and moving outward radially. Given the significant overlap that some of the topics have, however, such an organization is only for practical purposes. Further, it should be emphasized that although the research of the members of the WG is represented in this report, the research reported here is not limited to the WG and considerable effort has been made to include the work of scientists regardless of whether they are in the WG.

4.1.1 Introduction

Since IWTC-VII four years ago, there have been considerable research advances regarding the topic of TC structure and structure change processes. The focus of this report is on such changes excluding those resulting during the extratropical transition (ET) of TCs, which is the focus of Section 4.2 “Advances in understanding ET.” The research advances described below occur in all aspects of research: observations, theory, and modelling. Further, the results are aided by three significant field experiments that took place since IWTC-VII: NSF’s The Pre-Depression Investigation of Cloud-systems in the Tropics (PREDICT), NASA’s Genesis and Rapid Intensification Processes (GRIP) Experiment, and NASA’s Hurricane and Severe Storm Sentinel (HS3) Experiment – even though those field experiments targeted genesis and intensity change, foci of other WGs.

The divisions in regions of a TC are gray at best and make organization of a report such as this difficult. Accordingly, the organization outlined below is for practical reasons only and do not imply strict meteorological process separation among them:

- 4.1.2 *Formation of the TC eye*
- 4.1.3 *Slope of the TC eyewall*
- 4.1.4 *Structure and location of the TC warm core*
- 4.1.5 *Secondary TC eyewalls and eyewall replacement cycles (ERC)*
- 4.1.6 *TC convective asymmetry and spiral bands*

- 4.1.7 *Terrain impacts on TC structure*
- 4.1.8 *TC outflow and relationship to radial structure*
- 4.1.9 *TC size, size change, and new size/structure climatologies*
- 4.1.10 *Summary and recommendations*
- 4.1.11 *References*

Throughout this report, the WG's contributor's last name brackets the discussion submitted - although the original contributions have been edited slightly or split to improve flow and continuity. In cases where figure quality is unavoidably poor, the reader is recommended to refer back to the original published work from which the figures came.

4.1.2 Formation of the TC eye

The TC eye is the most noteworthy structural feature of a mature TC. Yet, Vigh et al. (2012) provided the first comprehensive climatology of hurricane eye formation (Figures 1 and 2). The following summary of that work is an abbreviated version of the Conclusions of that paper. They synthesized a new structure and intensity dataset from over 4600 vortex data messages (VDM)s, the best-track (BT) and extended best-track (EBT) datasets, and the SHIPS development dataset. Together with an archive of IR satellite images, they analyzed these data to determine the times at which each eye development baseline was observed. Of the 183 TCs that were reconnoitered by aircraft in the North Atlantic basin between 1989 and 2008, 70 TCs formed eyes and possessed sufficient data to be included as cases. The major findings and resulting physical insight of the climatology are:

- a) Banding is a precursor to eye formation. Of the 62 TCs that displayed banding prior to the formation of any eye, 51% later developed an aircraft eye.
- b) About 60% of TCs develop an eye during their lifetime.
- c) It has been generally thought that the convective ring of the developing eyewall should be apparent to aircraft before the eye is observed by satellite. This was indeed the case: for the TCs observed by both aircraft and satellite, the aircraft eye was reported before the satellite eye (IR3) in most cases (83%). This suggests that eye structure may develop first at lower levels (where it is more likely to be reported as an aircraft eye). Only later does the eye structure usually become observable in the cloud field (as seen from above).
- d) Aircraft eyes form at intensities that are considerably lower than hurricane intensity. Aircraft reported the first eyes at a wide range of intensities, but the median BT v_{max} is 58 kt (30 ms^{-1} ; central pressure of 991 hPa). This key finding may seem to contravene the conventional wisdom that the appearance of an eye marks the cyclone's crossing of the hurricane intensity threshold; however, this result is still broadly consistent with the Dvorak technique under the interpretation that the formation of a lower-tropospheric convective ring likely occurs well before the upper-tropospheric subsidence is strong enough to clear out the eye
- e) Eyes tend to form in environments that are conducive to further intensification of the TC.
- f) Sixty percent of storms formed their initial eyes within 48-h of undergoing genesis. This bolsters the Dvorak model of development, in which the typical TC increases from T2.5 (35 kt, 18 ms^{-1}) to T4.5 (77 kt, 40 ms^{-1}) over two days.

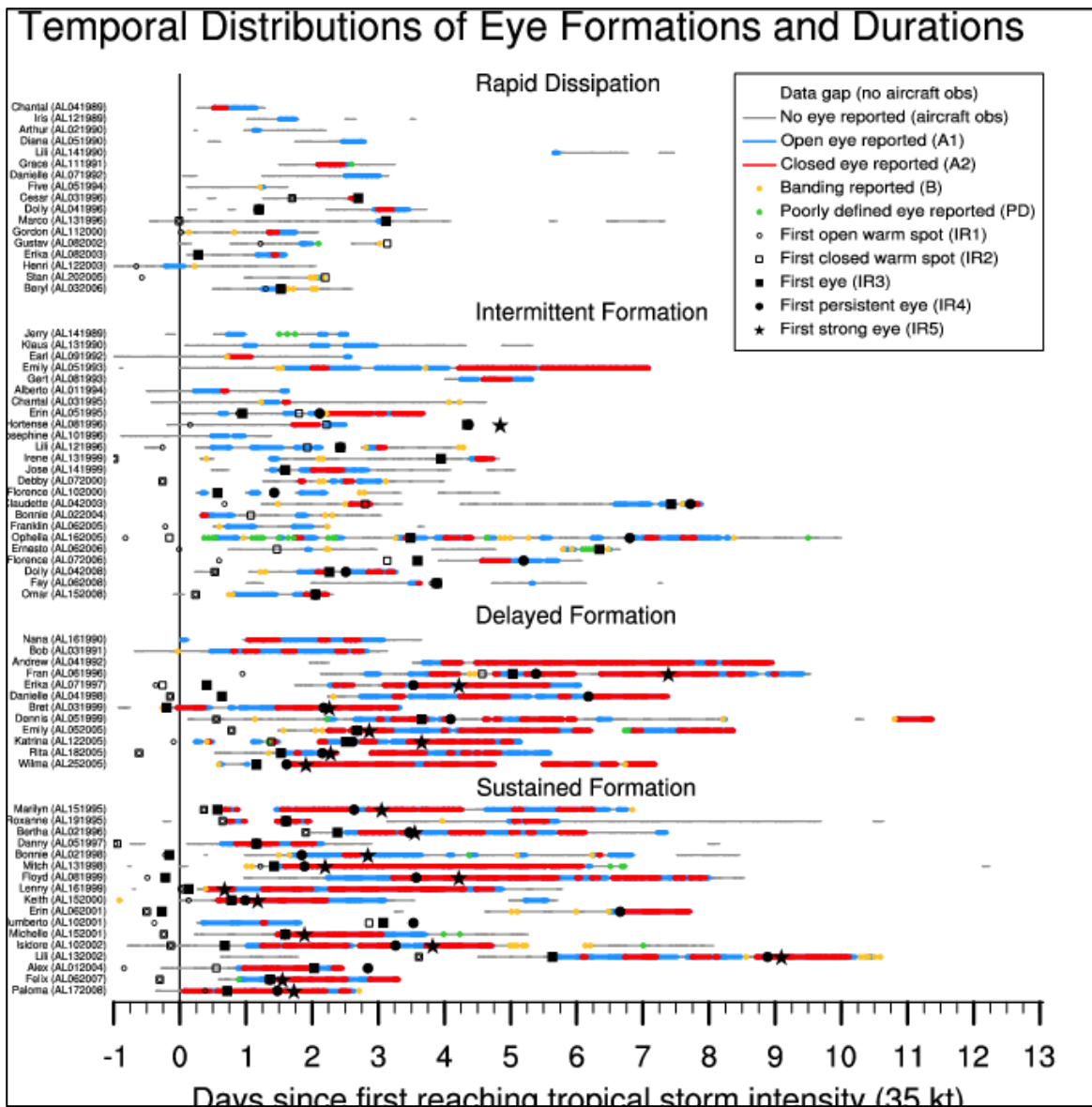


Figure 1. Temporal distribution of all Atlantic TCs that formed eyes during the period of aircraft reconnaissance.

TC timelines are grouped into the following case types: (a) “rapid dissipation,” (b) “intermittent formation,” (c) “delayed formation,” and (d) “sustained formation.” Line colours for each storm’s timeline indicate the following: data gaps of 12 h or greater that occurred within the reconnaissance period (white), periods when the TC was regularly reconnoitered, but an eye was not reported (gray), periods of active reconnaissance when an open eye was reported (blue), and likewise, periods when aircraft reported a closed eye (red). Orange dots indicate specific fixes in which aircraft reported banding (but not an eye), while green dots indicate fixes in which a poorly defined eye was reported. Additionally, polymarkers indicate the times when a TC first attained the following stages of IR eye development: open warm spot (IR1, hollow circle), closed warm spot (IR2, hollow square), first eye (IR3, filled square), first persistent eye (IR4, filled circle), and the first strong eye (IR5, filled star).

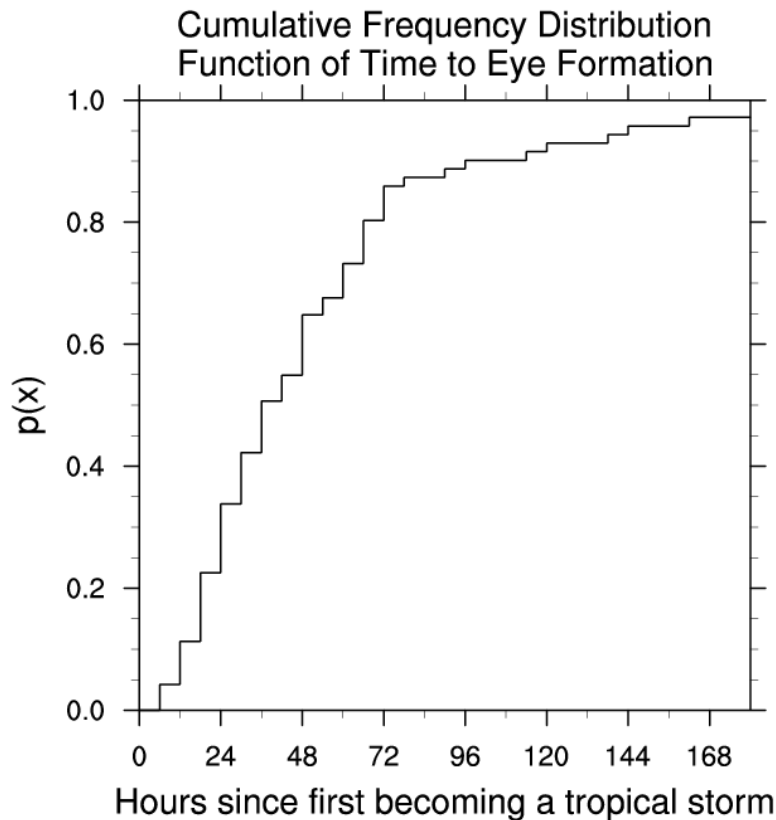


Figure 2. Cumulative frequency distribution of the probability of forming an eye. Time is measured relative to the first point that a system becomes a tropical storm according to the best track. The time of eye formation is taken to be the first report of an aircraft eye.

4.1.3 Slope of the TC eyewall

That a TC's eyewall tilts outward with height has been known for decades. It is a consequence of the warm-core nature of the cyclone, with the pressure gradient weakening with height (and thus the wind speed under geostrophic or gradient wind balance) – resulting in a parcel moving outward under the assumption of absolute angular momentum conservation and a lack of significant buoyancy (Emanuel 1986). However, even under these latter restrictions, there is quite a bit of variance permitted for the slope of the eyewall as the vertical and radial temperature gradients (which lead to the pressure gradients) vary from storm to storm (See Section 4.1.4). Further, the introduction of buoyancy from regional increases in sea-surface-temperature (SST) can provide parcel acceleration upward, and radially inward, from the angular momentum surface. All of these influences and potential departures from balance beg the question of what determines the eyewall tilt, and how that tilt is related to intensity and intensity change, as discussed at length next.

(**STERN**) Stern and Nolan (2009, hereafter SN09) utilized Doppler radar wind analyses obtained from NOAA's Hurricane Research Division to create a homogeneous dataset of azimuthal-mean tangential winds for seven hurricanes on 17 different days (this study was also mentioned in IWTC-VII, but is described here in order to provide context for the current summary). With this dataset, they re-examined three conventional wisdoms regarding the vertical structure of the radius of maximum winds (RMW):

- 1) That the outward slope of the RMW *decreases* (more vertical) with increasing intensity,
- 2) That the outward slope of the RMW *increases* with increasing RMW, and

- 3) That the RMW is approximately a surface of constant absolute angular momentum (M).

SN09 showed that (1) is actually false (there is no significant relationship between the slope of the RMW and storm intensity), whereas (2) was confirmed (the slope of the RMW increases linearly with the RMW itself). They found that while the RMW is indeed approximately an M surface, there is a systematic decrease of M upwards along the RMW. In addition to that observational evidence, SN09 utilized Emanuel's analytical vortex model (1986) to show theoretically that the slope of the RMW should increase linearly with size and be independent of intensity, and that the RMW should be closely approximated as an M surface.

Stern and Nolan (2011, SN11) used the same dataset as SN09, to examine the rate at which the maximum azimuthal-mean tangential winds decrease with height. They found that most storms have very similar vertical profiles of normalized maximum tangential winds (defined as the maximum at each height divided by the maximum at 2 km height). There is a small but systematic dependence of these vertical profiles on storm intensity and size: the percentage decay rate with height of maximum tangential winds *decreases* with increasing intensity, and *increases* with increasing RMW. SN11 showed that in the context of Emanuel's (1986) theory of maximum potential intensity (MPI), the percentage decay rate of maximum tangential winds should be essentially independent of both RMW and intensity, while the decay rate should *decrease* with increasing *potential* intensity. Using a suite of idealized WRF simulations, SN11 found that above the boundary layer, the normalized maximum tangential winds were generally independent of both intensity and RMW (consistent with theory). Within the boundary layer, they found that normalized maximum tangential winds *increase* strongly both with increasing intensity and increasing RMW. This relationship is *entirely* a consequence of the fact that the magnitude of supergradient winds increases systematically with intensity and RMW, as the profiles of the maximum *gradient* winds exhibit no such sensitivity.

Stern et al. (2014; hereafter S14) expanded the original dataset of SN09 (increasing the number of cases from 17 to 39), and revisited the analyses of SN09 and SN11. This more robust sample largely confirmed these earlier studies, finding that the slope of the RMW increases linearly with its size, and is uncorrelated with intensity (Figure 3). S14 also found that the slopes of the eyewall M surface, the eyewall updraft, and the 20-dBZ reflectivity isosurface all increase with their respective sizes. The 20-dBZ isosurface was previously examined by Hazelton and Hart (2013), and they found that the slope decreased with increasing intensity. While S14 found a marginally significant relationship between dBZ slope and minimum surface pressure, this was dependent on a single outlier, and the relationship between slope and maximum wind speed was insignificant. S14 did find that the observed slope of M decreases with increasing intensity (Figure 3). No measure of eyewall slope was found to have any relationship with intensity change. As in SN11, S14 found that the maximum azimuthal mean tangential winds decrease by (on average) about 20% from 2 to 8 km height, and that the percentage rate of decrease with height is slower for stronger storms and for smaller storms. Some storms exhibit an atypical vertical profile of maximum tangential winds, with a region of *increasing* winds with height from 2 to 4 km. S14 hypothesized that this anomalous structure is due to the effect of unbalanced flow, and presented evidence from the idealized simulations of SN11 that supports this idea (Figure 4).

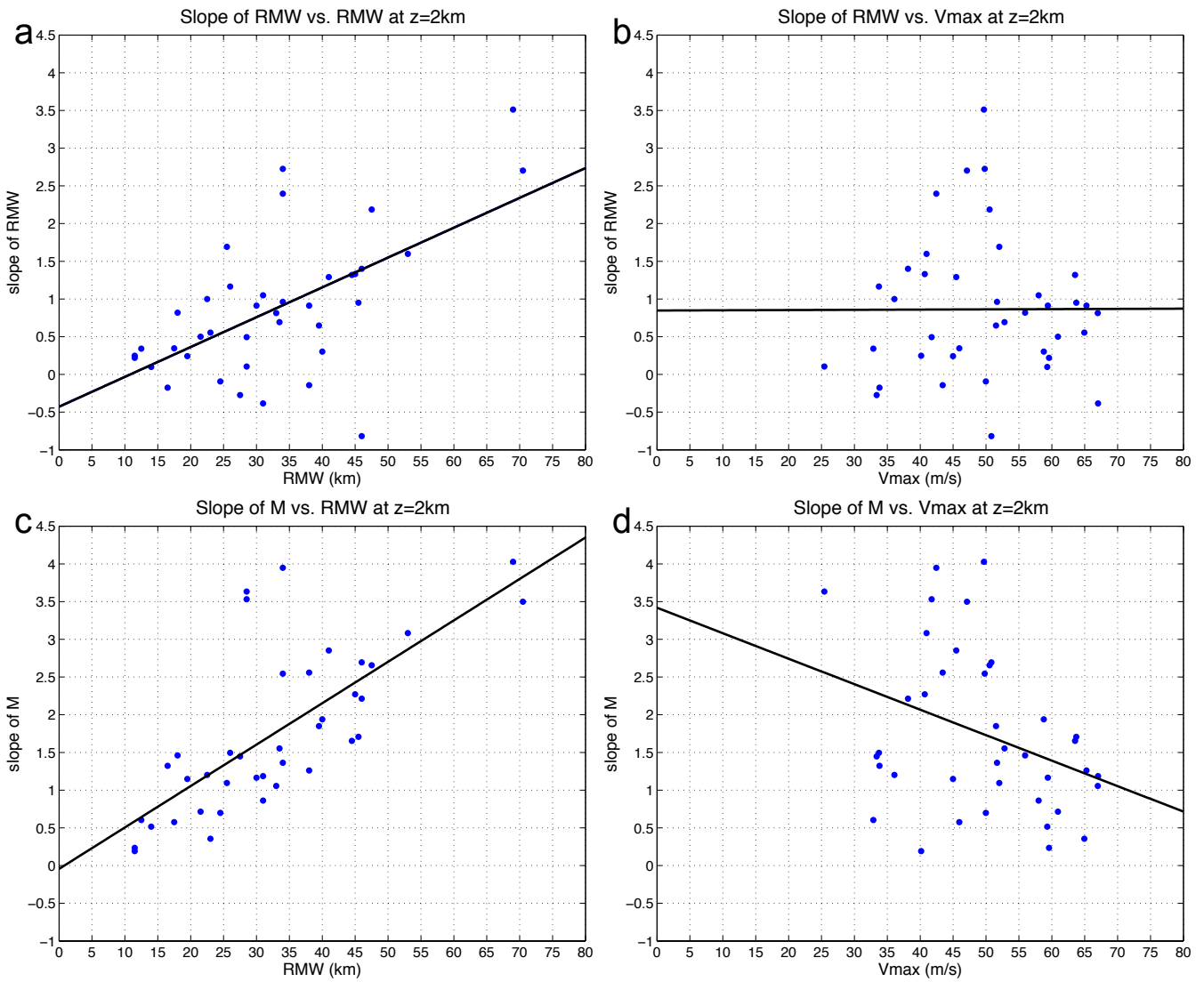


Figure 3. Figure 2 from Stern et al. (2014). (a) Slope of the RMW vs the RMW at 2-km height, (b) slope of the RMW vs the maximum azimuthal-mean tangential wind at 2-km height, (c) the slope of the M surface originating at the 2-km RMW vs the RMW at 2-km height, and (d) slope of the M surface vs the maximum azimuthal-mean tangential wind at 2-km height. The black solid lines indicate the best fit to the data.

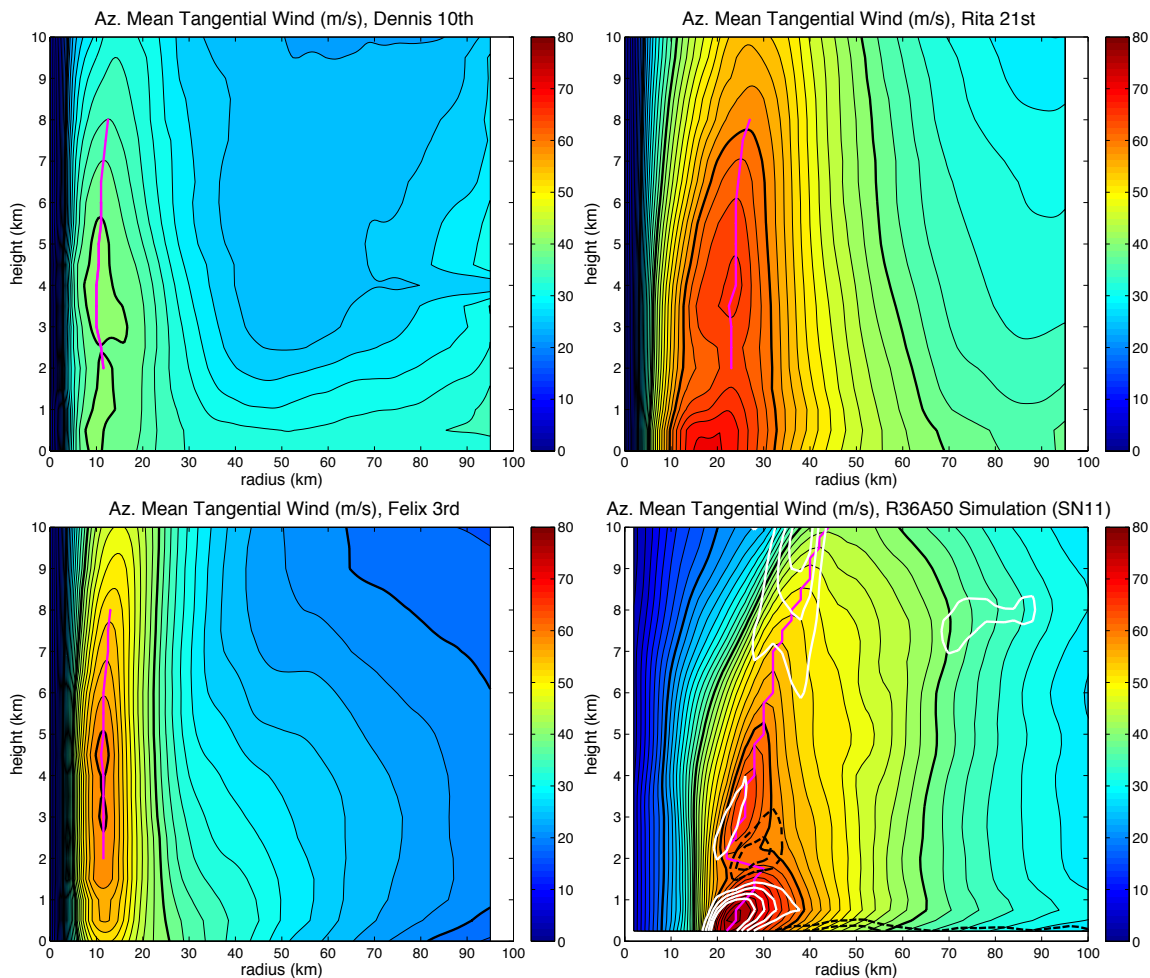


Figure 4. Figure 11 from Stern et al. (2014). Azimuthal-mean tangential wind for Hurricanes (a) Dennis on 10 Jul 2005, (b) Rita on 21 Sep 2005, and (c) Felix on 3 Sep 2007, and (d) the R36A50 simulation of SN11. The magenta line indicates the RMW. In (d), supergradient winds are contoured in solid white at +2, +4, +6, and +8 m/s, and subgradient winds are contoured in dashed black at -2, -4, -6, and -8m/s. Note that (d) is similar to Figure 17a of SN11.

As previously mentioned, Hazelton and Hart (2013) investigated the slope of the eyewall 20 dBZ reflectivity isosurface, using a dataset of airborne radar from 15 TCs. They found that the slope increases (becomes more outward) as intensity decreases (Figure 5) and as the radius of the eyewall increases. The relationship between slope and intensity is stronger than that found by S14, who found a very weak relationship using minimum surface pressure and a statistically insignificant relationship using maximum wind speed. These discrepancies are likely due to methodological differences or sample size or selection differences between these two studies. In agreement with S14, Hazelton and Hart (2013) found no relationship between intensity and eyewall size within their dataset.

Because Hazelton and Hart (2013) assessed the slope from individual radius-height cross-sections, they were also able to examine how slope varied with azimuthal location relative to the environmental vertical wind shear vector. They found that slope was slightly greater downshear as compared to upshear (**STERN**). Further details on that work and comparisons to the prior work follow.

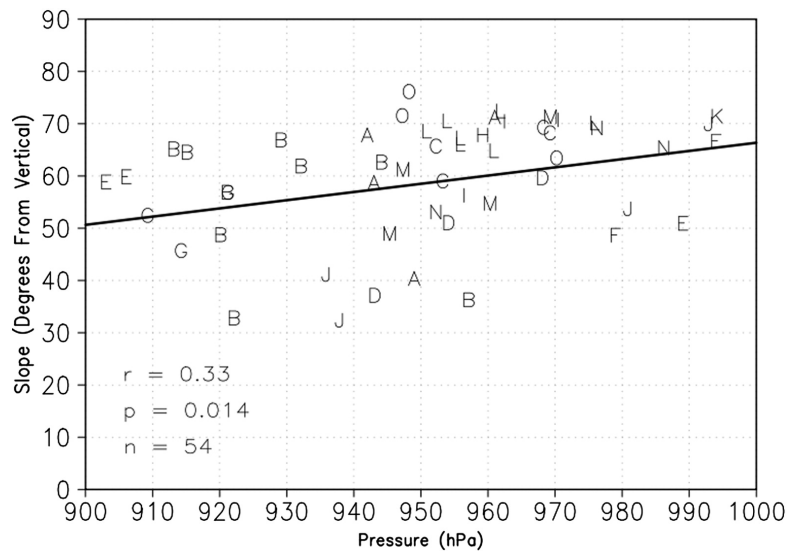


Figure 5. (Fig. 5 from Hazelton and Hart (2013)): Slope of the 20 dBZ isosurface vs. the minimum sea-level pressure. Each letter represents a single storm (given in Table 3 of Hazelton and Hart (2013)). Original Caption: The relationship between eyewall slope and minimum central pressure, with slope measurements averaged around the BT times and the pressure taken from the BT data. A letter represents the points for a single storm (defined in Table 3), and the scatter of points of the same letter show how the relationship is valid for the set of points as a whole, and is not simply a result of “clustering” from a few storms.

(HAZELTON) Hazelton and Hart (2013) used data from the three-dimensional Doppler Radar composites from the NOAA Hurricane Research Division P-3 flights into TCs (Gamache 1997, Reasor et al. 2009). The current dataset covers 75 flights into 19 TCs, but only a little more than half of these have a well-developed core region and sufficient azimuthal radar coverage near the core of the TC. The data typically only has good coverage up to 8-10 km, especially for the Doppler velocity data. This dataset has been used for several other analyses of TC core structure (e.g. SN09, Rogers et al. 2013, Reasor et al. 2013).

The average azimuthal mean slope of the 20 dBZ contour for 15 TCs analyzed by Hazelton and Hart (2013) was $dr/dz = 1.60$, more tilted than the azimuthal mean RMW slopes found by SN09 and S14. The slope of the 20 dBZ surface showed a statistically significant correlation overall with TC intensity ($r = -0.41$, $p < 0.01$). The relationship between slope and eye size was even more significant ($r = 0.56$, $p < 0.01$). These relationships are illustrated in Figure 6, which shows the evolution of the azimuthal mean reflectivity in Hurricane Felix over a period of approximately 24 hours. It can be seen that the 20 dBZ surface extended significantly higher into the troposphere and became more upright with time as the updrafts in the TC became stronger. In addition, the contraction of the eye is evident. During this time, Felix rapidly intensified from a Category 1 Hurricane with winds of 33 m/s to a Category 5 hurricane with winds of 77.3 m/s. The slope-intensity and slope-size relationships were obscured, however, by cases where an eyewall replacement cycle caused the inner eyewall updraft to weaken, but the inner eye did not totally collapse and the storm did not weaken for 6+ hours.

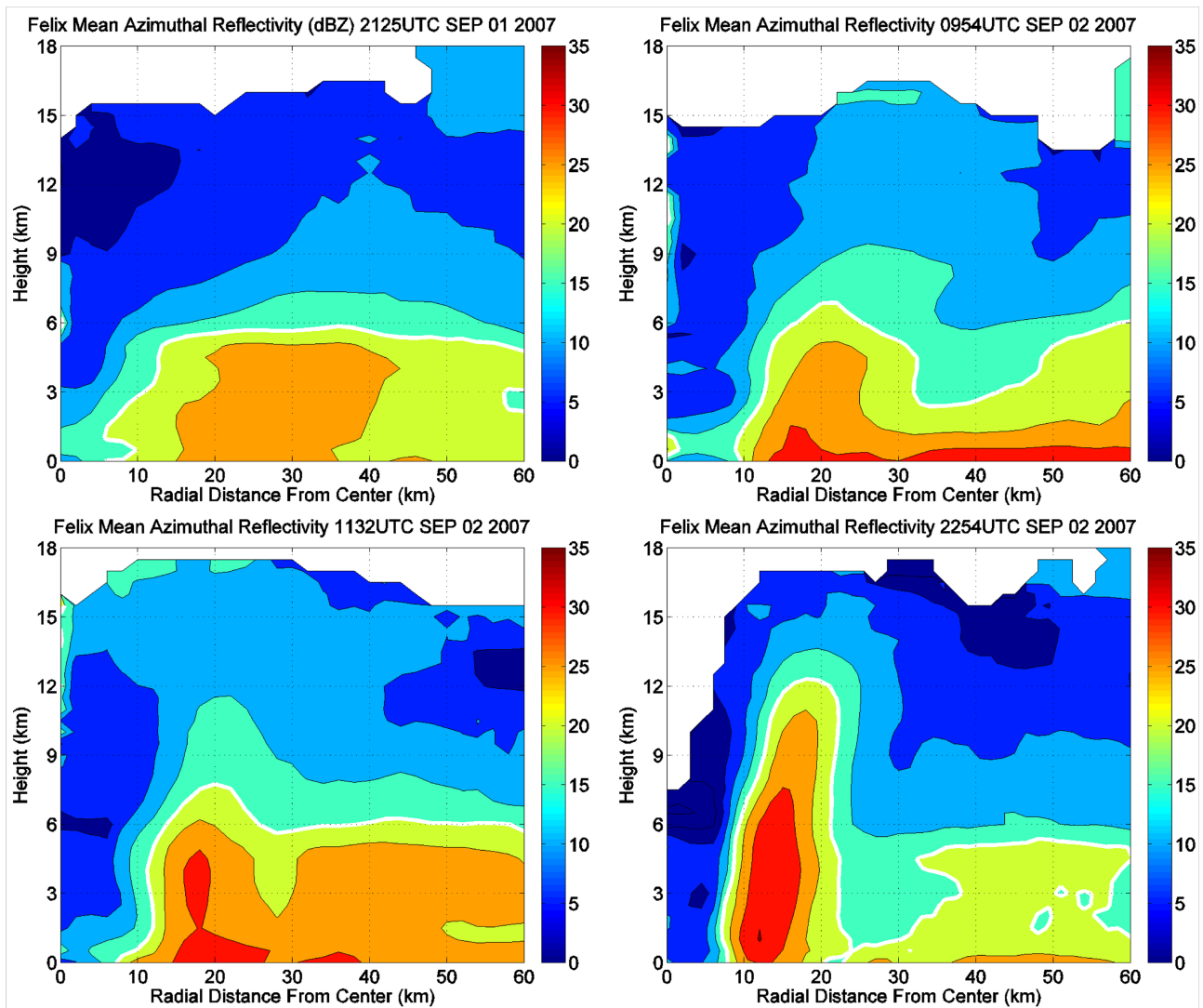


Figure 6. Azimuthal mean reflectivity (dBZ) for Hurricane Felix (2007) at four different times: 2125 UTC 01 September, 0954 UTC 02 September, 1132 UTC 02 September, 2254 UTC 02 September

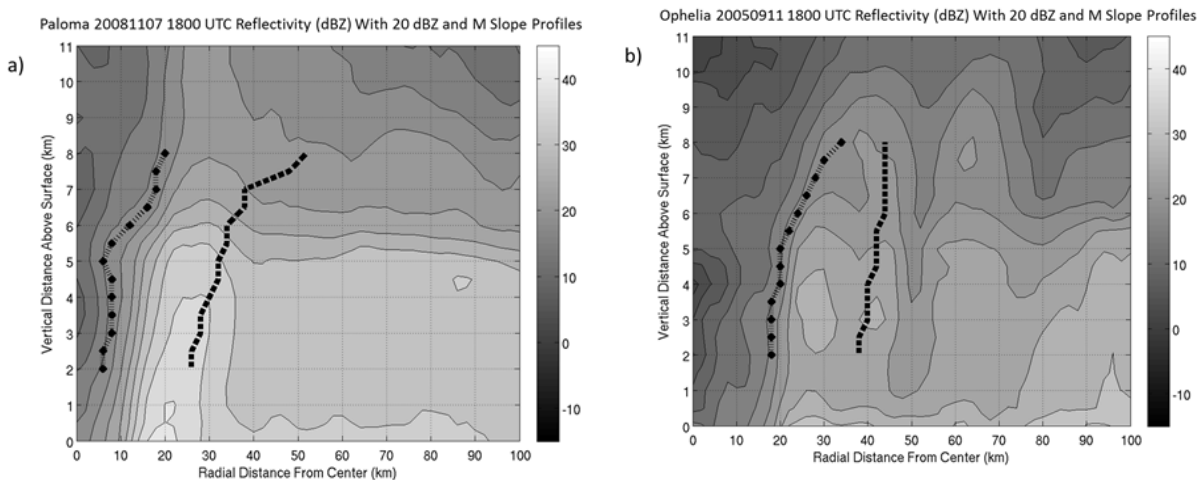


Figure 7. Reflectivity in the downshear-left quadrant, with M slope profile (dashed) and 20-dBZ slope profile (dot-dash) shown for a) Hurricane Paloma at 1800 UTC 7 November 2008 and b) Hurricane Ophelia at 1800 UTC 11 September 2005

Hazelton et al. (2014) next examined the variability of slope around the eyewall, in a shear-relative framework. The 20 dBZ surface was once again considered, as well as the RMW and the slope of the M surface passing through the RMW. The RMW tended to slope more on the downshear side than the upshear side of the eyewall, with a mean downshear slope (dr/dz) of 1.15 and a mean upshear slope (dr/dz) of 0.45. This azimuthal variance in RMW slope showed a connection to shear magnitude – the variance of the slopes was statistically significantly higher for cases where the shear was greater than 7 m/s. While M and dBZ slope did not show as much of a direct along-shear asymmetry, the difference between M slope and dBZ slope was found to be an important factor in distinguishing between intensifying TCs and weakening/steady TCs. For intensifying TCs, the dBZ surface in the downshear-left and upshear-left quadrants tended to be more upright than the M surface, indicating diabatic heating inside the local RMW. For weakening or steady TCs, however, the dBZ surface tended to be more sloped. This is illustrated in Figure 7, which shows downshear-left reflectivity and the dBZ and M surfaces in Hurricane Paloma (2008), which intensified by 25 knots in the following 12 hours, and Ophelia (2005), which weakened by 5 knots in the following 12 hours. These results are consistent with analysis of vertical motion for intensifying TCs by Rogers et al. (2013) **(HAZELTON)**.

4.1.4 Structure and location of the TC warm core

There has been a renewed interest in the structure of the warm core in recent years, in particular regarding the vertical structure of the perturbation temperature within the eye. Stern and Nolan (2012) and Stern and Zhang (2013a,b) showed that in idealized numerical simulations, the maximum perturbation temperature was consistently located at mid-levels (4-8 km height), substantially lower than what is widely believed to be a preferred upper-level (10-14 km) maximum. These studies also argued that existing observations are too sparse to determine a “typical” warm core structure, and that both the mean structure and its variability are poorly known. More detailed examination of these and other results follow.

(STERN) In a series of papers, Stern and Nolan (2012, SN12), and Stern and Zhang (2013a,b; SZ13a,b), used idealized numerical simulations to examine the thermodynamic structure of the eye, focusing in particular on the height of the warm core and the mechanisms that are responsible for warming the eye. Using a suite of simulations with varying initial storm structure as well as microphysics parameterization schemes, SN12 found that the maximum perturbation temperature in the eye was generally found at 4-8 km height. They also found that there was no systematic relationship between the height of the maximum and storm intensity. This mid-level maximum is in contrast to the conventional view that an upper-tropospheric (>10 km) maximum is typical. SN12 argued that due to the paucity of well-observed cases, the typical structure is actually not well known, and through a literature review showed that there exists some observational and numerical support for a mid-level maximum.

SZ13a followed up on SN12 by investigating the physical processes that warm the eye. Using a potential temperature budget analysis of an idealized simulation, they found that during the period of rapid intensification (RI), the greatest warming occurs at mid-levels, and this causes the maximum perturbation temperature to always be maximized in this region. SZ13a found that in their simulation, the warming of the eye during the beginning of RI occurred as a result of eddy radial advection, and not mean subsidence, as there was actually upward motion in the mid-level eye. During the latter part of RI, mean vertical advection was responsible for warming the eye. SZ13a showed that the mid-level maximum in warming was a result of the vertical structures of mean descent and static stability. As the static stability exhibits a relative maximum at mid-levels, moderate descent is able to accomplish substantial warming. Although descent is consistently maximized at 12-13 km height, the static stability is minimized there, and so advective warming is relatively small. Static stability rapidly increases with height in the tropical tropopause layer, and SZ13a concluded that this was responsible for a secondary maximum in the perturbation

temperature that was often found in this region in their simulations. SZ13b extended the analyses of SZ13a by simulating TCs under the influence of environmental vertical wind shear. The presence of shear itself does not substantially alter the evolution and structure of the warm core, and in particular, shear does not systematically alter the height of the warm core.

Durden (2013) then improved our observational understanding, by compiling and analyzing 18 eye soundings (from 9 storms on 16 different days) from high-altitude dropsondes, as well as 9 soundings (from 9 storms on 9 different days) from radiosondes. While all of these observations were pre-existing, most had never previously been published. Durden (2013) found a wide variability in the height of the maximum, ranging from 750 to 250 mb. In addition, he found that there is some tendency for the height of the maximum to increase with increasing intensity (although the scatter is quite large; Figure 8). Finally, Durden (2013) showed that the structure of perturbation temperature (and the height of the maximum warm core) can be sensitive to the chosen environmental reference profile, consistent with SN12.

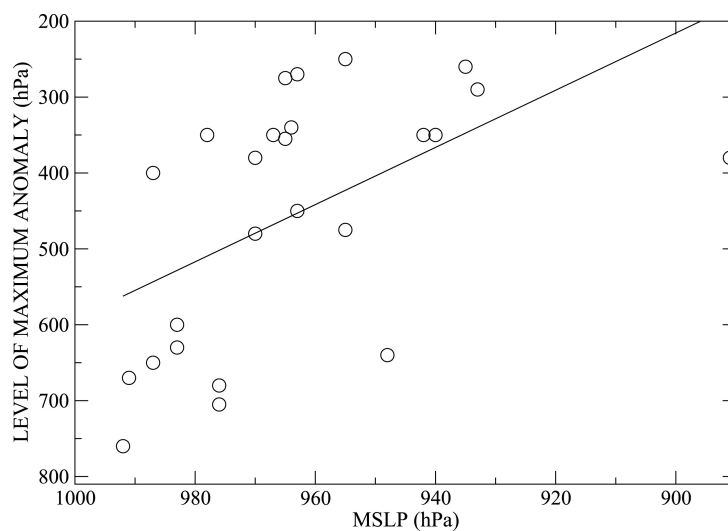


Figure 8 (Fig. 19 from Durden (2013)): Pressure of maximum perturbation temperature vs. minimum sea-level pressure, for the dropsonde and radiosonde dataset of Durden (2013).

Original Caption: Pressure height of the maximum temperature anomaly vs MSLP.
Solid line is the linear regression fit to the data.

Dolling and Barnes (2012, 2014) used dropsondes to analyze the evolution of the warm core structure in Hurricane Humberto (2001). They found that on 3 different days (with intensity ranging from Tropical Storm to Category-2), the maximum perturbation temperature was at low-levels (2-3 km). Although the data only extended to 10 km height, the perturbation temperatures above 5 km were consistently 2-4 K less than at low-levels. The authors argued that differential advection of dry air due to vertical wind shear prevented substantial warming from occurring at upper levels.

A different perspective on the TC warm core is seen in a series of studies by Chen et al. (2011) and Chen and Zhang (2013), who examined a simulation of Hurricane Wilma (2005). They found an upper-level (14 km) maximum in perturbation temperature in their simulation, and argued that the height of this warming caused Wilma to be more intense than it would have been otherwise, and that the formation of the upper-level warm core helped to trigger RI. This is in contrast to Stern and Nolan (2012), who argued that the height of the maximum perturbation temperature cannot be said to be the cause of intensity changes, and that there does not need to be a relationship between the height of the peak warming and intensity.

In a simulation of Super Typhoon Megi (2010), Wang and Wang (2014) found two prominent maxima in perturbation temperature, one at mid-levels (5-6 km), and another at upper-levels (15-16 km). The upper-level maximum did not form until a period of RI began (the intensity was already Category-2 at this point, however), and thereafter the greatest warming was at upper-levels, with a slight lowering of the height of the maximum with time during RI (from about 16 to 15 km). As in Chen and Zhang (2013), Wang and Wang (2014) attributed the upper-level warming in part to detrainment and descent from convective bursts that penetrate the stratosphere **(STERN)**. Further observational analysis and numerical modelling is needed to resolve the contrasts represented by the above suite of studies.

(STERN) In recent years, some progress has been made in our understanding of the factors that may influence the size of the inner core of TCs, although the relative importance of various processes remains unknown. One non-physical factor determining the RMW in numerical simulations is horizontal grid spacing, and (for example) Fierro et al. (2009) found that in simulations of Hurricane Rita (2005), the RMW systematically decreased as grid spacing was decreased from 5 km to 1 km. Hill and Lackmann (2009) used idealized simulations to show that the RMW increases with increasing environmental relative humidity, due to the increased convection and associated diabatic heating in outer rainbands. The idea that diabatic heating in outer rainbands is associated with an increased RMW is supported by Wang (2009) who used idealized simulations with artificial enhancement or suppression of heating to show that rainbands act to increase the size of the inner core. Another factor that appears to govern the size of the RMW is the initial size of the RMW and the initial radial profile of tangential winds outside of the RMW. Independently, Xu and Wang (2010) and Stern and Nolan (2011) found that in idealized simulations, the quasi-steady state size of the RMW increases with the initial size of the RMW. Stern and Nolan (2011) further found that quasi-steady state size increases with increasing broadness of the radial profile of tangential winds (i.e., storms where the wind decreases more slowly with radius beyond the RMW will eventually achieve a larger steady-state RMW than storms where the wind decreases more rapidly with radius).

Stern and Nolan (2011) also briefly noted that in their numerical simulations, contraction of the RMW in general was complete many hours (even days) before peak intensity was achieved (Figure 9). This phenomenon, which is somewhat in contrast to the existing paradigm whereby contraction and intensification occur simultaneously, was also seen to occur (but had not been noted) in a number of previous simulation studies. Some observational evidence for this relationship between contraction and intensification has been shown in Vigh (2010), who found that contraction tended to slow down markedly around the time of eye formation. Finally, Kieu (2012) found that in ensemble simulations of Hurricane Katrina (2005), contraction of the RMW was completed during the middle of RI, and further intensification occurred at a fixed RMW **(STERN)**.

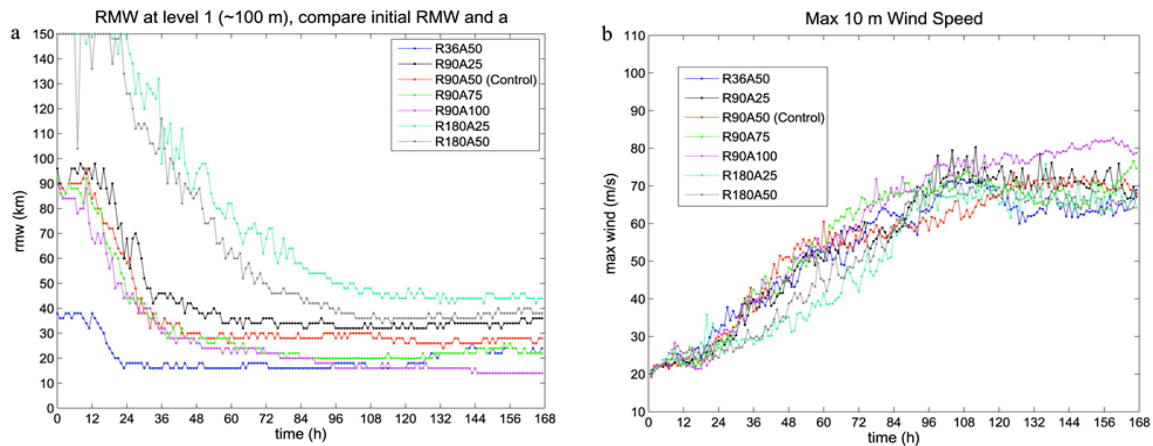


Figure 9. (Fig. 13 from Stern and Nolan (2011)): For simulations with varying initial RMW and radial profile of tangential winds outside of the RMW, time series of (a) the RMW at the lowest model half-level (~100 m) and (b) the maximum 10-m wind speed. The initial RMW for each simulation is given (in km) by the number following “R” in the legend, and the initial radial profile of tangential winds is indicated by the number following “A” in the legend (see Stern and Nolan (2011) for details). “A25” is the broadest profile (slowest decay with increasing radius) and “A100” is the sharpest. Original Caption: For the simulations with varying initial RMW and a, time series of (a) the RMW at the lowest model half-level (~100 m) and (b) $V_{max_{10}}$. For the R180 simulations, the RMW is first found inside of our 150-km radial domain near 0000 UTC on day 2.

4.1.5 Secondary TC eyewall formation and eyewall replacement cycles

Secondary eyewall formation (SEF) is one of the most important problems in the topic of structural change of mature TCs, but as of yet there is no consensus on the phenomenon’s fundamental physics. Nonetheless, there has been a substantial amount of research since the past IWTC conference that is examined next, including the occasional revisit on the relevant prior work.

(ABARCA) Today our best secondary eyewall forecasting efforts rely on statistical tools (Kossin and Sitkowski 2009) and we are yet to include the fundamental physics of the phenomenon in such efforts. In the last four years there have been numerous studies of secondary eyewalls based on theory, observations and numerical models of various complexities. These studies have either adopted an axisymmetric perspective or have aimed to understand the role of asymmetries. From the axisymmetric perspective, some studies have argued that generalizations of the Ekman balance are an adequate framework to describe secondary eyewall formation and, as it follows from such theory, the boundary layer contributes rather than initiates SEF (Kepert 2013; Kepert and Nolan 2014). In contrast with such view Rozoff et al. (2012) and Zhu and Zhu (2014), emphasize the crucial role of outer rainband heating in SEF, in the context of the balanced dynamics of (Shapiro and Willoughby 1982). Aligned with this view, Sun et al. (2013) proposed that SEF ultimately arises from convective heating (in the context of balance dynamics), but acknowledges some positive feedback with boundary layer dynamics. Another view, proposes that boundary layer, unbalanced dynamics, are an essential component of the secondary eyewall formation processes (Wu et al. 2012; Huang et al. 2012; Bell et al. 2012). Abarca and Montgomery 2013; 2014a; 2014b) have quantitatively argued that while the balance component contributes to secondary eyewall formation, it is largely insufficient to explain secondary eyewall spin up. Yet, another view, articulated in Williams et al. (2013) advances the idea that shock-like structures can be the primary control on the location and strength of the deep convection in secondary eyewalls.

On the role of asymmetries, substantial and perhaps contradictory studies have been published. Montgomery and Kallenbach 1997; Qiu et al. 2010; Martinez et al. 2010; Menelaou et al. 2012; Abarca and Corbosiero 2011 have proposed that Vortex Rossby Waves (VRW) can impact the inner core of the tropical cyclone in such a way that results in secondary eyewall formation, while Judt and Chen (2010) have found no evidence of VRW links to SEF (**ABARCA**).

(HUANG) The role of the boundary layer dynamics on SEF has been investigated by two recent studies (Wu et al. 2012; Huang et al. 2012; hereafter WH12) based on the two mechanisms for the spin-up of azimuthal-mean tangential winds in single-eyewall TCs highlighted in Smith et al. (2009). By assimilating T-PARC (THORPEX-Pacific Asian Regional Campaign; Elsberry and Harr, 2008) data (in particular, the aircraft observations) into the WRF (Weather Research and Forecasting) model based on ensemble Kalman filter data assimilation, Wu et al. (2012) constructed a model/observation- consistent and high-resolution spatial/temporal dataset for Typhoon Sinlaku in the first of two companion works. The following features were robustly identified in the storm's outer-core region around one day before SEF:

- 1) The horizontal broadening of low-level tropospheric swirling flow;
- 2) Intensification of boundary layer inflow over the outer region. These two important features are consistent with flow characteristics indicated in the two mechanisms highlighted for the spin-up of single-eyewall TCs, and set the scene for a progressive boundary layer control pathway to SEF.

In the second of the two companion papers, Huang et al. (2012) addressed the association between increases in storm size and SEF from the axisymmetric viewpoint. Their findings point to collective structure changes in the outer-core region of a mature TC (Figure 10), which ultimately culminates in the formation of a secondary eyewall. The sequence begins with the broadening of the low-level tangential wind field associated with the intensification of the eyewall that can be demonstrated by the balanced response above the boundary layer. Due to the presence of surface friction, boundary layer inflow increases underneath the broadened swirling wind, and becomes large enough to enhance the swirling circulation within the boundary layer. This rapid increase in tangential winds near the top of the boundary layer breaks the gradient wind balance, leading to the local development of supergradient winds, which decelerate the inflow air parcels and impede their inward movement. This process leads to the transition outside the primary eyewall from sporadic and/or weak convergence in the lower troposphere to a well-defined convergence zone concentrated within, and just above, the boundary layer. This progressive increase in supergradient forces continuously provides a mechanical means for high-enthalpy air to erupt from the boundary layer.

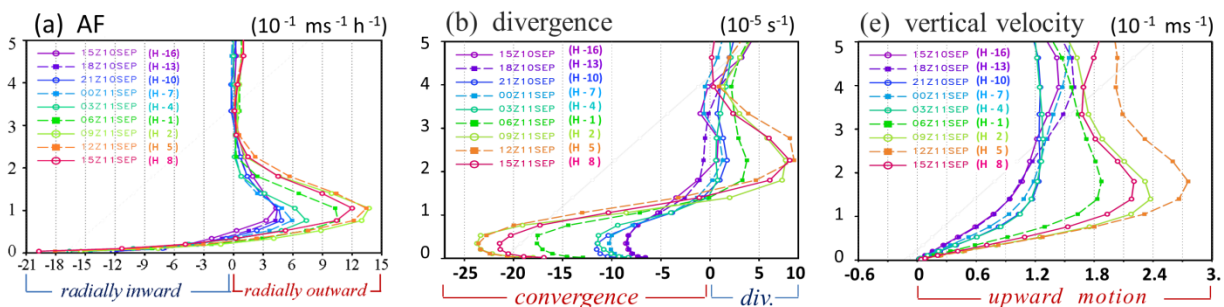


Figure 10. Vertical profiles of the azimuthally-, area-, and temporally- averaged gradient wind (m s^{-1} ; top), divergence (10^{-5} s^{-1} ; middle), and vertical velocity (10^{-1} m s^{-1} ; bottom) in the SEF region over ($t - 3 \text{ h}$, $t + 3 \text{ h}$). Results are shown from 16 h before SEF (H-16) to 8 h after SEF (H08).

Given the dynamically and thermodynamically favourable environment for convective activity, the progressive responses of the unbalanced boundary layer flow to an expanding swirling-wind field appear to be an important mechanism for concentrating and sustaining deep convection in a narrow supergradient-wind zone collocated with the SEF region. While understanding the importance of the balanced response, this study particularly pointed out the critical role of unbalanced dynamics in SEF. The presented progressive boundary layer control on SEF also implies that the boundary layer scheme, and its coupling to the atmosphere above, need to be adequately represented in numerical models to improve our understanding of SEF, as well as the accuracy of SEF forecasts, including the timing and preferred radial intervals.

The dynamical pathway to SEF advanced in WH12 is attractive on physical grounds, and its simplicity means that it is easy to examine (**HUANG**). This view has been supported by in-situ observations and further quantification based on numerical modelling.

(BELL). The ERC of Hurricane Rita (2005) was observed by multiple aircraft during the Hurricane Rainband and Intensity Change Experiment (RAINEX, Houze et al. 2006). The high-resolution structure of Rita's double eyewall was documented in Houze et al. (2007) but more detailed analysis of the structure change during the ERC has been conducted more recently. Didlake and Houze (2011) used Electra Doppler Radar (ELDORA) observations to show that the developing secondary eyewall is primarily strengthened through mean vortex stretching in the updraft just inside the secondary tangential wind maximum. A supergradient jet in this region decelerates the inflow, and a portion of the inflowing air then rises and moves radially outward. Locally intense convective cells create perturbation motions that lead to a negative vorticity tendency radially outside the jet largely through vertical advection of vorticity. The combination of mean updraft and perturbation convective scale motions act together to strengthen the tangential wind maximum and build the secondary eyewall.

Further analysis of Hurricane Rita by Bell et al. (2012) is consistent with the hypothesis that the secondary eyewall develops from the bottom-up through strong low-level convergence and vortex stretching. A comparison of the structure of Rita before and after secondary eyewall formation is shown in Figure 11. The azimuthally averaged kinematic fields from the ELDORA analysis at 1936 UTC 21 September (Figure 11a), 1838 UTC 22 September (Figure 11b), and their difference (Figure 10c) reveal the marked structural changes occurring in the vertical vorticity, tangential wind, angular momentum, and secondary circulation over 23 hours. A reduction in the vorticity, tangential wind, updraft, and inflow in the primary eyewall is accompanied by an increase in these quantities in the secondary eyewall. The Doppler wind analyses are consistent with dropsonde analyses that suggest the presence of supergradient winds in the boundary layer reducing the inflow to the primary eyewall and enhancing the convergence and updraft in the secondary eyewall. Observational evidence continues to mount for the presence and importance of boundary layer processes in ERCs (**BELL**).

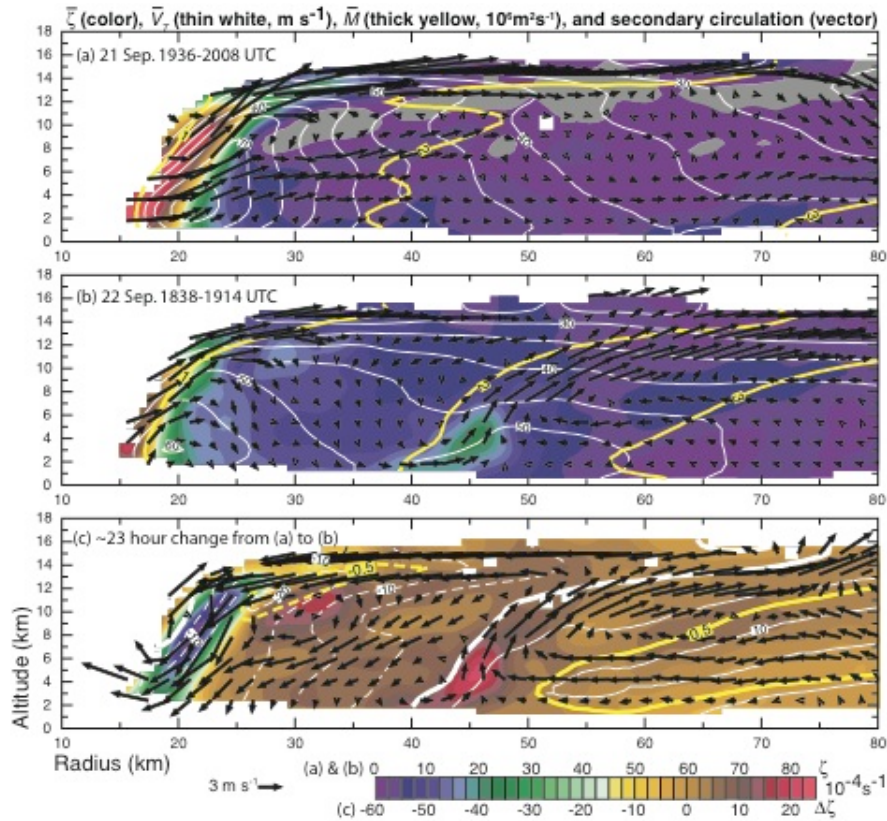


Figure 11. Axisymmetric relative vorticity (colour, 10^{-4} s^{-1}), tangential wind (contour, m s^{-1}), and secondary circulation (vector) derived from ELDORA. Dashed contours in (c) indicate a negative change of tangential wind and absolute angular momentum, thick contours indicate zero change, and solid contours indicate positive change. Vorticity change in (c) is indicated by the numbers on the bottom of the colour bar.

(**ABARCA**) Given the work of Huang et al. (2012) and the verification of it by Didlake et al. and Bell et al., Abarca and Montgomery (2013, 2014; hereafter AM13,14) focused on numerical modelling, capitalizing on the fact that state of the art, high-resolution, mesoscale models generate secondary eyewalls with remarkable similarity to those observed in nature (in situ observations often lack the spatiotemporal coverage needed in SEF studies). That research has combined (realistic and idealized) mesoscale numerical simulations (WRF and RAMS) with evidence from two other numerical frameworks. The first numerical framework is an axisymmetric, nonlinear, time-dependent, slab boundary layer model with radial diffusion; the second is the Sawyer-Eliassen equation, used to diagnose the secondary circulation of a vortex forced by diabatic heating and/or tangential momentum sources. Comparisons of the full-physics integrations with those of the Sawyer-Eliassen inversions (based on secondary circulation and derived tangential wind tendency) have been used as quantifications of the extent to which SEF processes depart from balance dynamics. The main contributions of these findings form the basis for a new view of SEF dynamics:

- a) Balance dynamics¹ are an insufficient framework to describe SEF, because they do not capture its tangential wind spin up (AM14). This conclusion results from comparing the azimuthally averaged secondary circulation (and corresponding tangential wind tendencies) between mesoscale integrations and those diagnosed as the axisymmetric balanced response of a vortex subject to diabatic and momentum forcings. An example of such comparison is shown in Figure 12.
- b) Boundary layer dynamics, as captured by a slab boundary layer model, are capable of developing secondary wind maxima (AM13). An example of such capability of a boundary layer model is shown in Figure 13.
- c) An analysis of the time-dependent slab model with a prescribed and time-independent forcing of tangential wind at the top of the boundary layer reveals that the simulated secondary wind maximum contracts inward, as secondary eyewalls do in mesoscale models and in nature, pointing to a hitherto unrecognized role of boundary layer dynamics in the eyewall replacement cycle.

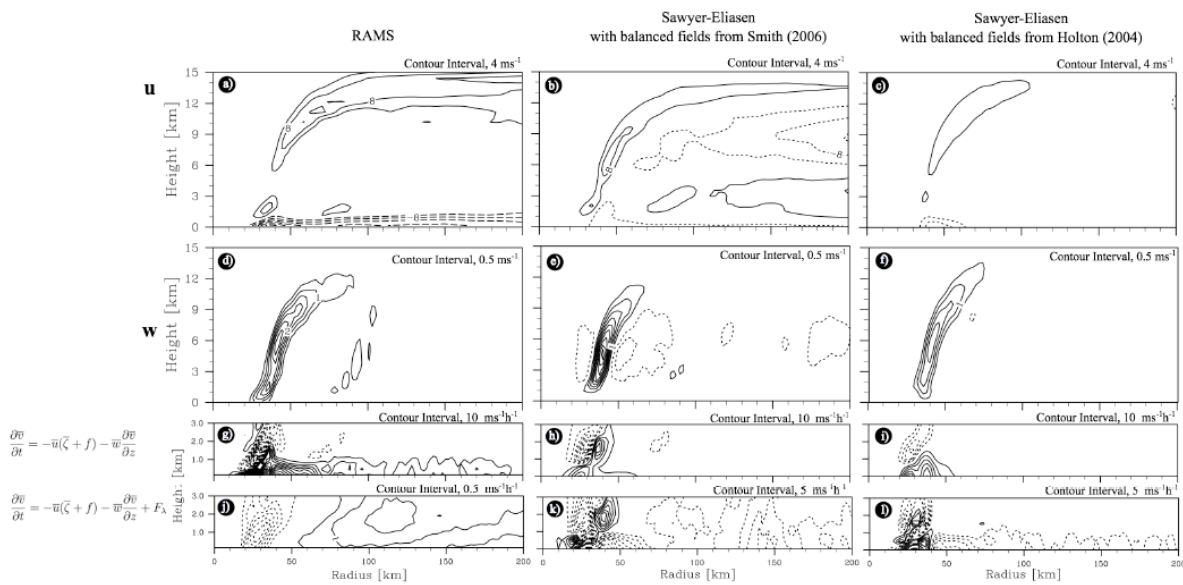


Figure 12. Vertical cross sections of the radial (top row) and vertical (second row) wind components and tangential wind tendencies (as defined in the left part of the figure, third and bottom rows); for the azimuthal averaged fields of the RAMS simulation at hour 174 (left column) and the Sawyer-Eliassen model integrated with balanced fields as in Smith (2006, centre column) and in Holton (2004, right column). See text for further details and definition of symbols in the left part of the Figure. Wind velocities are presented in m s⁻¹ and tangential wind tendencies in m s⁻¹ h⁻¹. Contour intervals are indicated in each panel. Adapted from AM14.

¹ Balance dynamics is defined here, following the tropical meteorology literature, as those processes that maintain a vortex in axisymmetric thermal wind balance. These dynamics capture the tropical cyclone intensification mechanism resulting from the radial gradient of the buoyancy generation rate in association with the aggregate latent heat release in deep convective clouds.

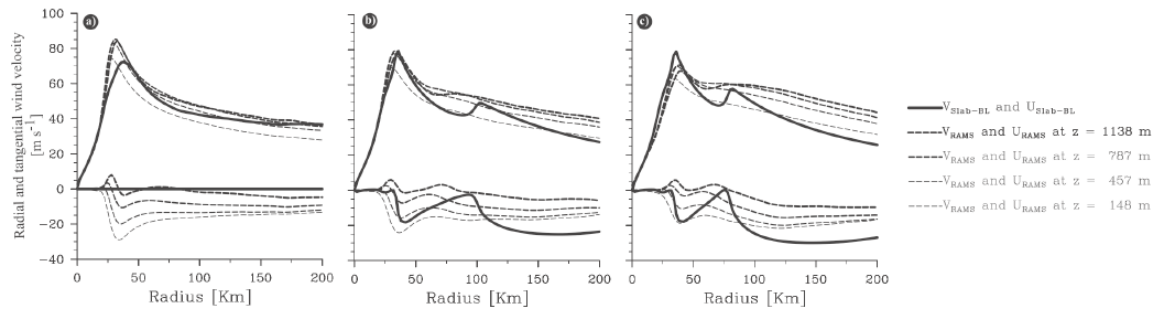


Figure 13. Tangential and radial wind field profiles of the mesoscale simulation after azimuthal and 2-h averages at the $z=1138$ -, 787 -, 457 -, and 148 -m model levels (dashed curves) and slab boundary layer simulations (instantaneous fields, solid black curves). (a) Wind profiles at hour 13 of the mesoscale simulation including the tangential wind profile at $z=1512$ m that is used as the initial condition for the slab model and forcing (solid curve; see text for details). (b) Mesoscale model profiles centred at hour 18 and the results of the slab model (solid curve) after 5 h of integration. (c) Mesoscale model profiles centred at hour 23 and the results of the slab model (solid curve) at 10 h of integration, when the slab model is reaching equilibrium. The figure shows that boundary layer dynamics, as captured by a slab boundary layer model, are capable of developing secondary wind maximum.

Adapted from AM13.

Related published works include an appraisal of a recent hypothesis for SEF (Montgomery et al. 2014). While most of the previously mentioned work in this contribution focused on axisymmetric views of the SEF problem, it also includes contributions on the asymmetric aspects of the problem. Abarca and Corbosiero (2011) study vortex Rossby wave occurrence prior to SEF and outline possible relationships between these two storm structures. Additionally, Terwey et al. (2013) discuss some aspects relevant in the study of vortex Rossby waves in the context of SEF (**ABARCA**).

(RAMA RAO) Wang (2012) in his recent review on TC structure and intensity explained that the development of a concentric eyewall and the subsequent eyewall replacement (usually termed the concentric eyewall cycle) are one of the major mechanisms that can result in rapid TC structure and intensity changes (Willoughby et al. 1982; Houze et al. 2007; Sitkowski et al. 2011). Observational studies have revealed that concentric eyewalls only form in intense TCs and the associated intensity change varies considerably from case to case and the concentric eyewall structure can persist ranging from a few hours to more than a day (Hawkins and Helveston 2008; Kuo et al. 2009; Kossin and Sitkowski 2009). Based on 10-yr (1997-2006) satellite data, Hawkins and Helveston (2008) reported that about 80% of TCs with a minimum central surface pressure lower than 940-950 hPa or the maximum surface wind greater than 50-60 m/s experience at least one concentric eyewall cycle in their life time over the western North Pacific while the ratio is reduced to 70% for the North Atlantic, 50% for the eastern Pacific, and 40% for the Southern Hemisphere. This indicates that in addition to the intensity, the particular regional environmental conditions could contribute to the formation of concentric eyewall structure as well. The intensity change in response to the eyewall replacement is found to be largely determined by the nature of the heating in the secondary eyewall (Zhou and Wang 2011a).

Recently India Meteorological Department (IMD) upgraded its operational HWRf system with EMC/NCEP upgraded 2013 version with improved resolution through addition of another storm following moving nest operating at cloud-permitting 3 km grid spacing with improved vortex initialization to match the observed storm size, structure and intensity. The recent real-time operational forecast with high resolution HWRf model over Bay of Bengal during 08-14 October 2013 for Very Severe Cyclonic Storm (VSCS) Phailin shown the model was able to capture the

observed structure of TC in its forecast when the system intensified from Cyclonic Storm (CS) to VSCS stage (Figure 14). The real-time HWRf model forecast evaluation over NIO during 2010-13 with vortex initialization has shown improvement in structure and intensity forecast by the model (Das et al. 2014) (**RAMA RAO**).

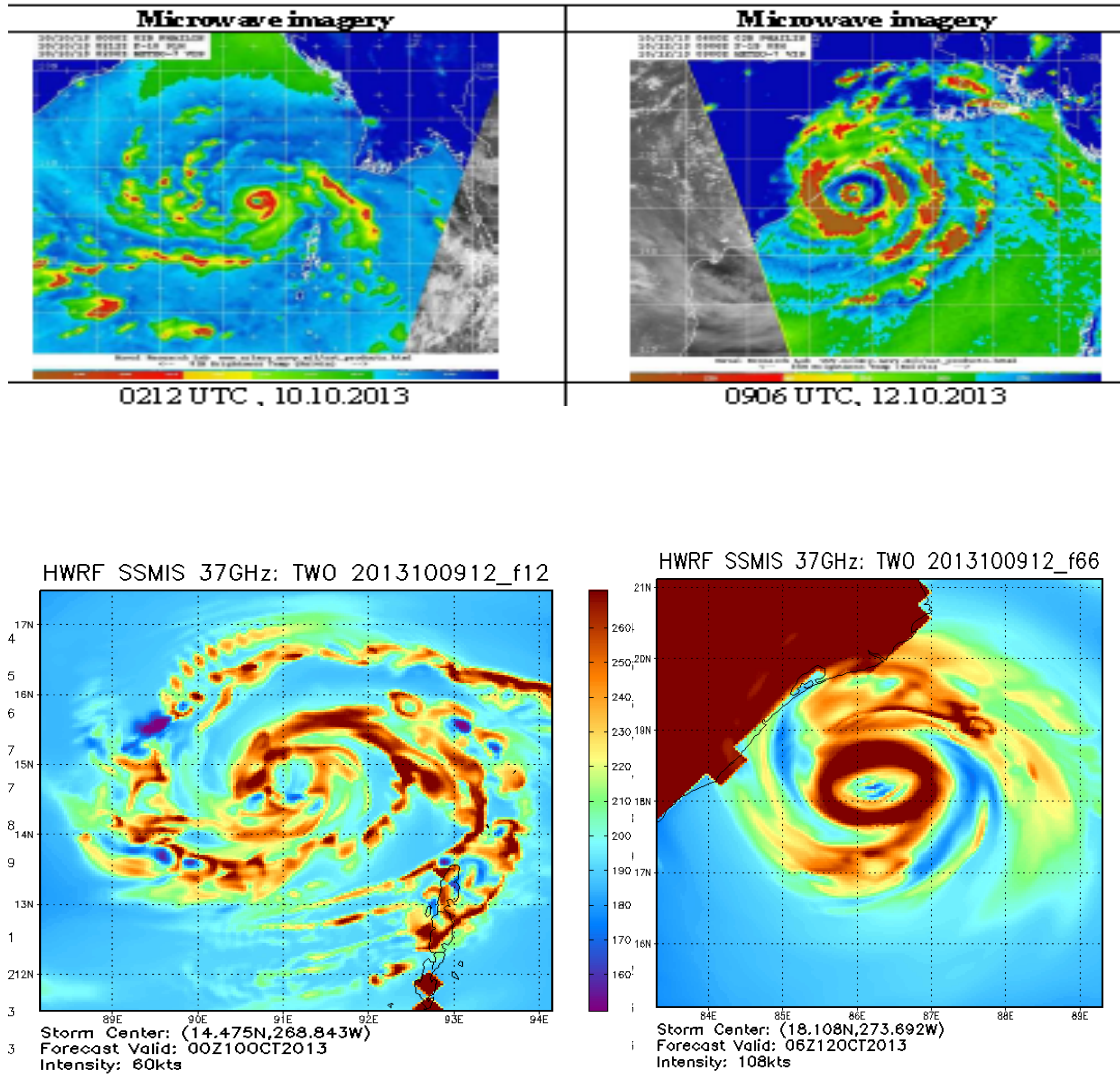


Figure 14. The high resolution HWRf model real-time forecast based on 12 UTC/09 October 2013 12h and 66h forecast valid for 00 UTC/10 October and 06 UTC/12 October and corresponding NOAA satellite microwave imageries when the system is CS and VSCS stages

From the foregoing review, it is clear that there are currently competing theories on the essential dynamics of secondary eyewalls and it would seem to be too early to adjudicate which, if any, of these theories most closely captures the phenomenon.

4.1.6 TC convective asymmetry and spiral bands

The report thus far has focused primarily on research progress in the area of axisymmetric structural features. Concurrent with these advances, considerable recent research progress has been made on the asymmetric structure processes in TCs, including the role of vertical wind shear (VWS) on TC convective asymmetry as well as the formation and evolution of TC spiral bands.

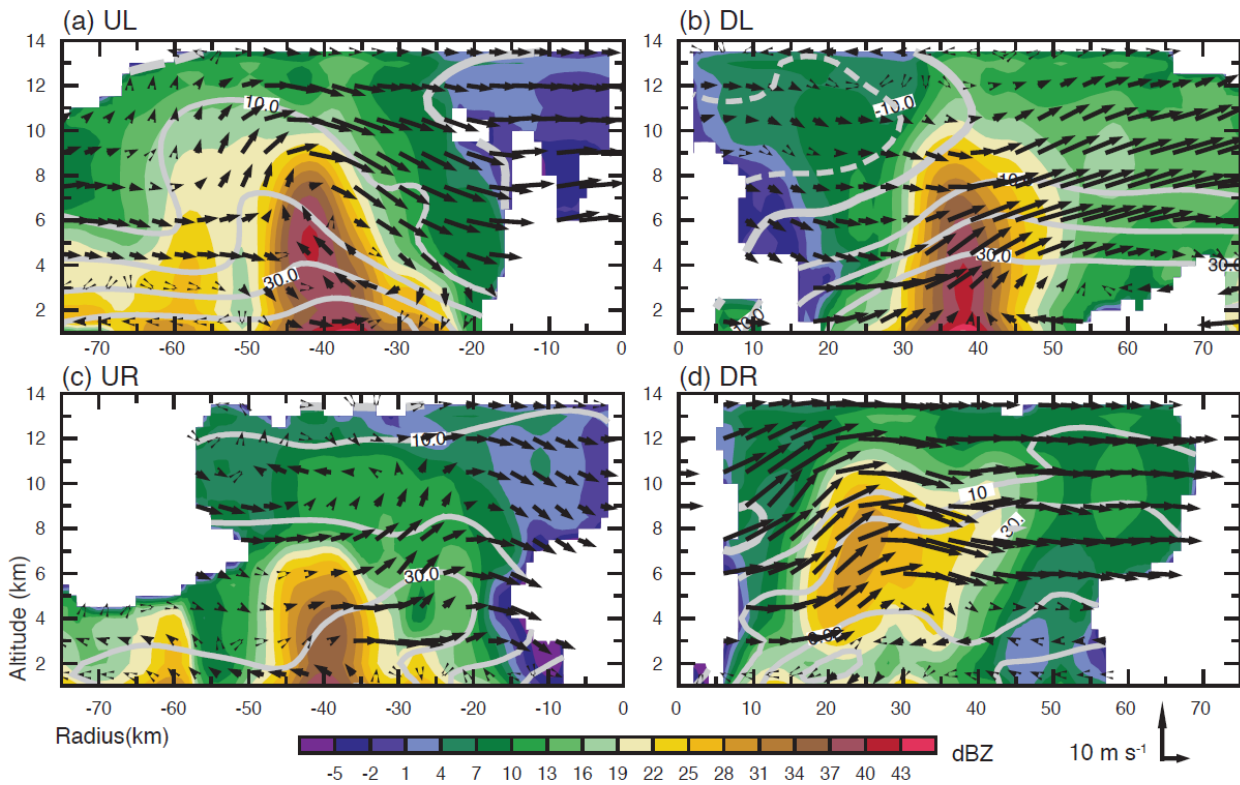


Figure 15. Vertical cross sections from ELDORA analysis of radar reflectivity in dBZ (shaded), tangential wind in m s^{-1} (gray contours), and in-plane wind vectors composed of radial and vertical velocity for each shear-relative quadrant in Typhoon Sinlaku on 19 September 2008. Cross-sections are taken from the corner of the domain to the typhoon centre, 45 degrees from the X and Y axes in each quadrant: (a) upshear left, (b) downshear left, (c) upshear right, and (d) downshear right. (From Foerster et al. 2014)

(BELL) Another important process for structure change is the influence of vertical wind shear (VWS) on the vortex and convective structure. While it is now well established that VWS induces asymmetries, observations of the detailed convective and kinematic structure of mature storms influenced by strong VWS have been limited. ELDORA observations of Typhoon Sinlaku (2008) during its entire life-cycle were collected during the combined THORPEX Pacific Area Regional Campaign and Tropical Cyclone Structure field experiment (T-PARC/TCS08). Sinlaku weakened after making landfall on Taiwan but then re-intensified due to a strong convective burst induced by moderate wind shear as it approached Japan (Sanabia 2010). The typhoon re-formed an eyewall as it recurved, with the resulting convective structure hypothesized to be due to variations in filamentation time (Kuo et al. 2012) not typically seen in stronger TCs.

Sinlaku continued to re-intensify as the VWS increased to over 13 m s^{-1} at 33°N latitude and the convection became highly asymmetric (Figure 15) (Foerster et al. 2014). The eyewall structure consisted of a convective initiation region in the downshear right quadrant, with active deep convection downshear left that matured and transitioned to stratiform convection in the upshear quadrants. The resulting convective structure resembled that of sheared TCs observed at lower latitudes, but with an enhanced stratiform region hypothesized to be due to the weaker intensity of Sinlaku. The relationship between VWS direction and asymmetric TC convective structure is consistent with other recent studies using satellite-derived precipitation data (Hence and Houze 2011), and airborne radar data (Reasor et al. 2013; DeHart et al. 2014).

Notably, the inner-core structure was still warm-cored in this transformation stage (Klein et al. 2000) prior to the interaction with the baroclinic zone to the north. The Sinlaku observations were not sufficient to evaluate the thermodynamic impacts proposed by Riemer et al. (2010, 2013) that shear-induced downdrafts flush the boundary layer with cool, dry air that act as “anti-fuel” for the TC heat engine. Frontal structure and extra-tropical characteristics became apparent on the following day as the storm passed north of Japan (Quinting et al. 2014) (**BELL**).

(**STOVERN**) Wang (2009) explored how outer spiral rainbands affect the TC inner core size and structure by artificially modifying the heating and cooling rates in the outer core precipitation field. They found that artificial warming in the rainbands lowers the pressure outside the core which in turn reduces the pressure gradient. The reduced pressure gradient is accompanied by a deceleration of the inner-core wind velocities, which momentarily slows down storm intensification but causes an expansion in the inner-core wind field. Conversely, cooling in the outer-rainbands increases TC intensity but allows the inner core to remain compact. It is concluded that the presence of strong, active outer spiral rainbands in a TC limits intensification but increases the TC inner core size. In this case, it is the hydrostatic adjustment from the diabatic heating outside the inner-core that facilitates the inner-core size change.

Xu and Wang (2010a) artificially removed the surface energy fluxes within various radii of a simulated TC in order to study the resulting effects on the inner-core size. Removing the surface fluxes within the eye region had little effect on the inner core size, showing only a slight increase in the RMW of the simulated storms. However, removing the surface entropy fluxes outside the eyewall resulted in a contraction of the inner-core wind field, defined as the area between the radius of maximum wind (RMW) and radius of 25.7 m/s or radius of damaging winds (RDW). An analysis of the angular momentum budget while using arguments from Wang (2009) revealed that eyewall contraction was primarily due to the increased radial pressure gradient force and inward penetration of accelerating boundary layer inflow across the RMW.

The expansion (contraction) of the inner-core wind field is explained by a positive feedback mechanism which is driven by the presence (lack of) of the surface energy fluxes (Figure 16). In their control simulation with unmodified surface fluxes, the boundary layer inflow that occurs outside the eyewall is controlled mostly by diabatic heating in the active spiral rainbands. Radial advection of angular momentum driven by the enhanced boundary layer inflow penetrates the inner core and increases the tangential winds outside the eyewall which leads to the outward expansion of the tangential wind field while increasing the absolute vorticity outside the RMW. In turn, the larger wind field enhances the surface fluxes outside the eyewall which continues to feed outer core convection and maintain the process.

In contrast, removing the surface fluxes outside the eyewall immediately reduces the convective available potential energy (CAPE) which suppresses the activity of spiral rainbands in the outer core, maintaining a strong PGF near the eyewall but limiting the boundary layer inflow outside the RMW. The TCs remain compact, radial advection of absolute vorticity is limited, and Ekman pumping is dampened which further suppresses outer rainband activity. The physical mechanisms resulting in the size changes are consistent with the mechanisms described by May and Holland (1999) and Hill and Lackmann (2009).

XW10b studied the effect that the initial vortex size has on the evolution of the inner-core size of a TC. They found that an initially larger vortex develops a larger inner-core with more spiral rainbands extending out to larger radii. An analysis performed on the azimuthal mean radial and tangential momentum equations showed that it is the radial advection of the absolute angular momentum via the vertical absolute vorticity term ($u\zeta_a$) that is the dominant mechanism responsible for the observed increase in the inner-core size of the simulated TCs. In their

simulations, the outward expansion rate of boundary layer inflow was proportional to the initial size of the vortex. Using arguments from XW10a and Wang (2009), they explained that a larger initial vortex has a stronger circulation outside the RMW than a smaller vortex of the same intensity and thus produces larger surface entropy fluxes outside the eyewall. This is favourable for the production of rainbands and the diabatic generation of potential vorticity. They found that spiral rainbands can result in and enhance the boundary layer inflow not only immediately outside the RMW but also at relatively large radii. The diabatically induced radial inflow brings large amounts of angular momentum into the inner-core region via the radial advection of absolute angular momentum, leading to an increase in tangential winds outside the eyewall and thus the outward expansion of the wind field and increase in the inner-core size.

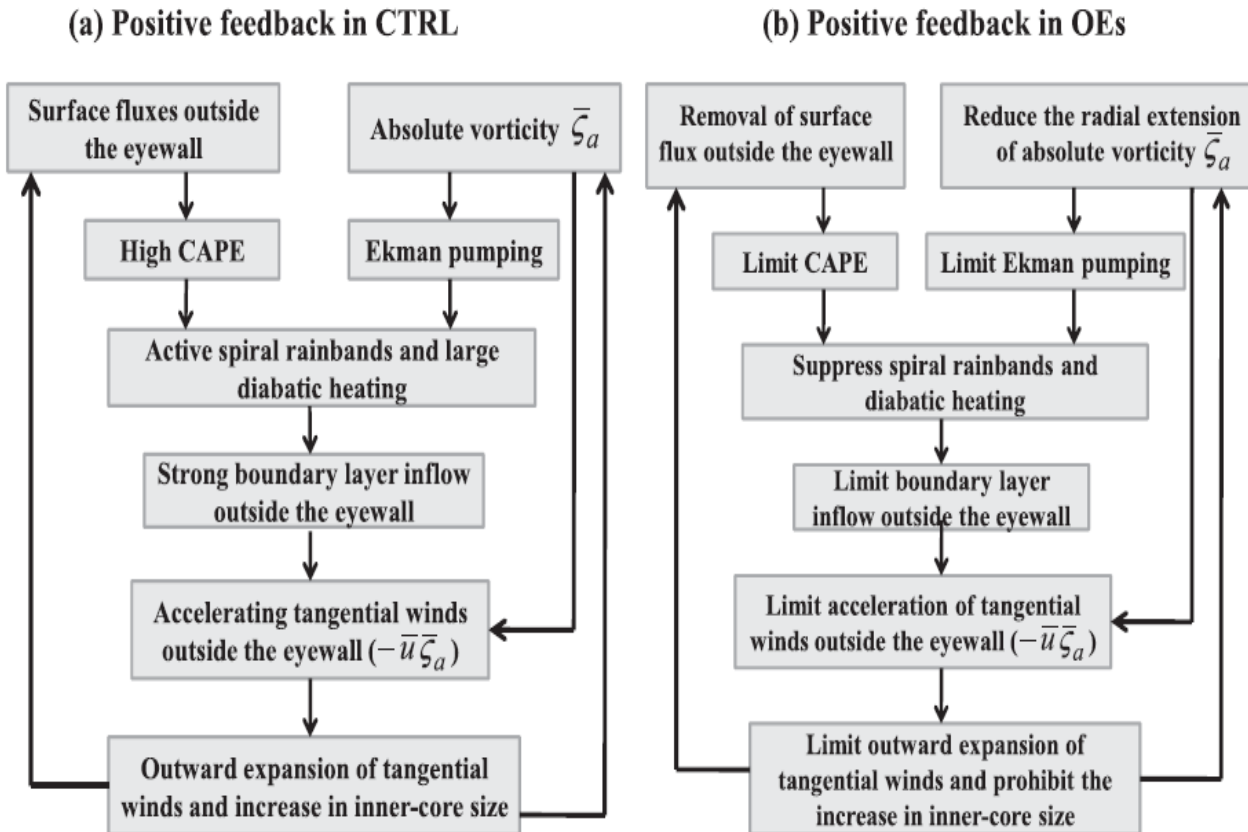


Figure 16. From Xu and Wang (2010a), a schematic showing the positive feedback responsible for (a) the increase in the TC inner-core size in the control and (b) the decrease in the inner core for simulated TCs with moisture fluxes systematically removed

Ying and Zhang (2012) found that abundant moisture supply in the TC outer core region is critical to the growth of the horizontal extent of the primary TC circulation. Motivated by the results of Wang (2009) and Hill and Lackmann (2009), they numerically simulated the lifetime of Typhoon Talim (2005) using the version 3.2.1 of the Weather Research and Forecasting modelling (WRF) using initial conditions from the NCEP final analysis dataset. They produced a suite of sensitivity experiments by modifying the water vapour mixing ratio fields in the northern and southern sectors of the TC and over the entire computational domain. They found that TC structure is highly sensitive to moisture variations in the north sector of the storm region. With the presence of more moist air, the TC develops more convection in the outer core yet intensification is reduced due to limited radial advection of angular momentum in the inner core. In contrast, with drier air in the inner core intruding from the northern sector, convection in the outer core is suppressed producing a more compact TC. They found that these results are consistent with those produced by Hill and Lackmann (2009) and Wang (2009) (**STOVERN**).

(RAMA RAO) Over the Bay of Bengal, Raghavan (1997) has reviewed the radar studies of the Indian TCs. Based on composite conventional radar reflectivity value he prepared a sketch of centre of TC, the eye, principal band and other spiral bands (also called rainbands). It also shows the pre-storm convection and outer rainbands. He pointed out that outer convective activity or outer rainbands are those band which are either poorly organized or in the stage of organization, but are ahead of the organized spiral bands. According to him precipitation elements are arranged in rainbands, which converge into the TC centre. He also noted that for the Bay of Bengal TCs south of 20° N, high value of reflectivity and maximum winds are packed in the left quadrant, while in most of Atlantic cyclones they are packed in the right front quadrant of the moving TC. He noted a deleterious effect of landfall on the structure of a TC as friction increased and latent and sensible heat fluxes were reduced. Mesocyclones and tornadoes may develop either in the eyewall region or in the rainbands upon a TCs landfall or in a rainband prior to landfall but upon its contact with land. These mesocyclones are seen highly localized and persistent reflectivity areas of a TC on radar **(RAMA RAO)**.

(SAWADA) To investigate a formation mechanism for spiral rainband, cloud-resolving simulations with 2-km mesh were conducted under idealized conditions. Convective cells produce cold outflows due to evaporative cooling near the surface, which form the convergence zone between cold outflows and inflows at low levels. The cold outflows force the inflows from the outside to lift up at the leading edge. New convective cells are successively generated at the upstream end of a convective cell, which are organized into the spiral-shaped rainband along the low-level inflows (Figure 17). On the other hand, outer rainband is formed with little cold pool when the environmental moisture is rich. Akter and Tsuboki (2012) showed from the simulation of Cyclone Sidr (2007) that low-level convergence within the band was caused by the deceleration of the cross-band component of a gradient inflow and non-gradient inflows. Rainband activity also has a significant impact on TC size through the diabatic heating. The diabatic heating generated by rainbands drives the secondary circulation and enhances inward transport of absolute angular momentum around the mid-troposphere, increasing the TC size. This is consistent with other works, Fudeyasu and Wang (2011). They demonstrated that the contribution of diabatic heating to spin-up of outer core circulation of a simulated tropical cyclone and the diabatic heating in the mid-upper-tropospheric anvil clouds plays a dominant role **(SAWADA)**.

(MOON) This two-part study examined spiral rainbands in a numerical simulation of Hurricane Bill (2009). Moon and Nolan (2014a; Part I) evaluated the structures of spiral rainbands and compared them to previous observations. The innermost domain of the Hurricane Bill simulation had 624×624 points of 1-km horizontal grid spacing and 61 vertical levels. The Weather Research and Forecasting model version 3.2.1 was used for the Hurricane Bill simulation with standard parameterization physics. Model outputs from the 1-km domain were produced every two minutes starting at simulation hour 36 for 24 hours (i.e., between Hour 36 and Hour 60).

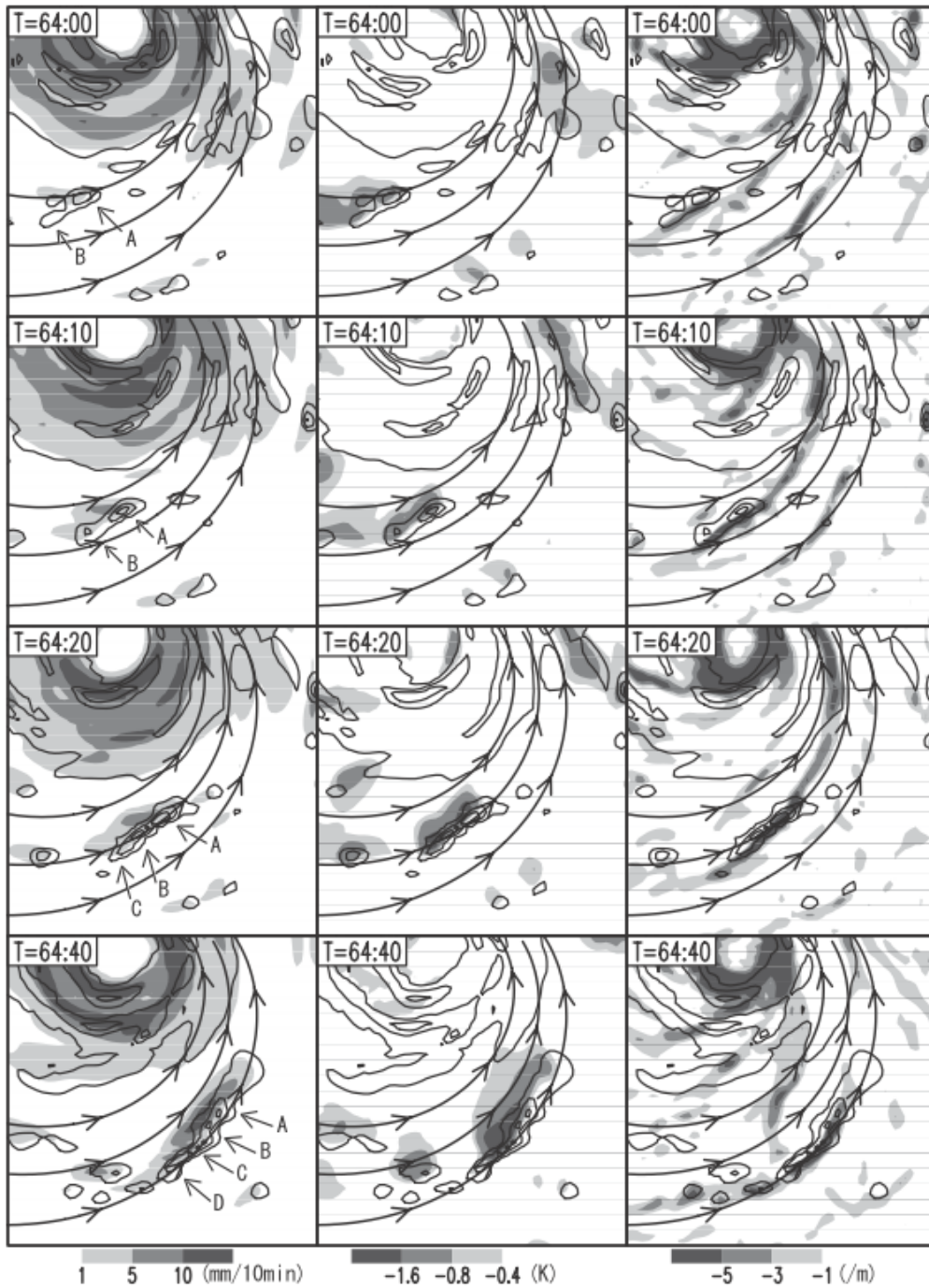


Figure 17. The rainband formation from 64 h to 64 h 40 min over a domain of $120 \times 120 \text{ km}^2$ in the control experiment. Contours depict horizontal distribution of vertically accumulated rainwater with contour values of 2, 10, and 30 kg m^{-2} . Shaded areas display (left) precipitation, (middle) potential temperature anomaly from an azimuthally averaged temperature at 20-m height, and (right) horizontal convergence. Thick solid lines with arrows are streamlines azimuthally and temporally averaged at a height of 260 m.

Four types of spiral rainbands were identified: principal, secondary, distant, and inner rainbands. Principal rainbands tended to be stationary relative to the storm centre, while secondary rainbands were more transient and moved around the storm centre. Both principal and secondary rainbands were tilted radially outward with height and had many of the commonly observed kinematic features, such as overturning secondary circulation and enhanced tangential velocity on their radially outward sides, as documented in previous observational studies (e.g., Barnes et al.

1983; Powell 1990a,b; Hence and Houze 2008; Didlake and Houze 2009, 2013a,b). Principal rainbands were bounded by very dry air on their radially outward sides (see Figure 8b of Part I). Distant rainbands were radially inward-tilting convective features that have dense cold pools near the surface (see Figure 8c of Part I). Inner rainbands were made of shallow convection that appeared to have originated from near the eyewall. However, even at this model resolution, the Hurricane Bill simulation could not realistically reproduce some of convective-scale features such as indirect overturning circulations on the radially inward sides of outward-tilted principal and secondary rainbands.

The focus of Moon and Nolan (2014b; Part II) was inner rainbands, which typically form just outside the eyewall and propagate radially outward with time while being advected around the storm centre. This paper evaluated whether the propagation of inner rainbands in the Hurricane Bill simulation was consistent with previously proposed hypotheses such as gravity waves, vortex-Rossby waves, or squall lines.

This paper found that the propagation of inner rainbands was not consistent with gravity waves because inner rainbands were not consistently collocated with vertical velocity (or pressure) signals expected if these rainbands propagated like gravity waves. In addition, inner rainbands did not have dense surface cold pools that were typically associated with squall lines, so it was unlikely that inner rainbands propagated like squall lines.

Surprisingly, the propagation of inner rainbands was not found to be consistent with vortex-Rossby waves (VRWs) in this paper. Montgomery and Kallenbach (1997; MK97) first showed that VRWs propagated radially outward with time from the core region of the tropical cyclone-like, basic-state vortex along the negative potential vorticity (PV) gradient outside its radius of maximum wind (RMW) and hypothesized that inner rainbands were the manifestation of VRWs. Using linearized shallow-water equations, MK97 also presented the properties of their propagation and interaction with the basic-state vortex.

Subsequent studies provided evidence that the propagation of inner rainbands was consistent with VRWs. Corbosiero et al. (2006) analyzed radar observations of Hurricane Elena (1985) and noted an inner rainband that propagated radially outward with time (see their Figure 7). This rainband was well captured by the azimuthal wavenumber-two ($n = 2$) component of radar reflectivity. The time evolution of a cross section through this feature (see their Figure 11) revealed that the radar reflectivity feature associated with the rainband clearly propagated radially outward with time, and its radial phase speed was found to be consistent with the VRW theory. Chen and Yau (2001) and Wang (2002) presented evidence that the propagation of inner rainbands was consistent with VRWs in numerical simulations of tropical cyclones. They found that inner rainbands were collocated with positive PV anomalies and higher reflectivity signals and the phase speeds of PV anomalies associated with the rainbands were consistent with the VRW theory.

Figure 18 shows horizontal cross sections at $z = 3.2$ km of reflectivity every 4 minutes between 0900 UTC and 0920 UTC of August 20 from the Hurricane Bill simulation. During this period, an inner rainband located to the southeast of the storm centre appeared to propagate radially outward with time. The $n = 2$ decomposition of reflectivity appeared to capture the radial outward propagation of this rainband well.

VRWs are PV bands that emanate radially outward from near the eyewall along the sharp negative PV gradient. If the propagation of inner rainbands has a physical connection to VRWs, there should be some clear correlations between PV bands and inner rainbands. Figure 19 shows horizontal cross sections at $z = 3.2$ km of $n = 2$ PV and $n = 2$ reflectivity during the same period as in Figure 18. They indicated that the positive part of the $n = 2$ reflectivity associated with the

rainband (thick solid black lines) was not collocated with the positive part of the $n = 2$ PV. Instead, a dipole-like structure of the $n = 2$ PV was collocated with the positive part of the $n = 2$ reflectivity during its radially outward propagation. Horizontal cross sections of PV at the same time and height as in Figure 18 also showed horizontal dipoles of PV associated with the rainband (see Figure 6 of Part II).

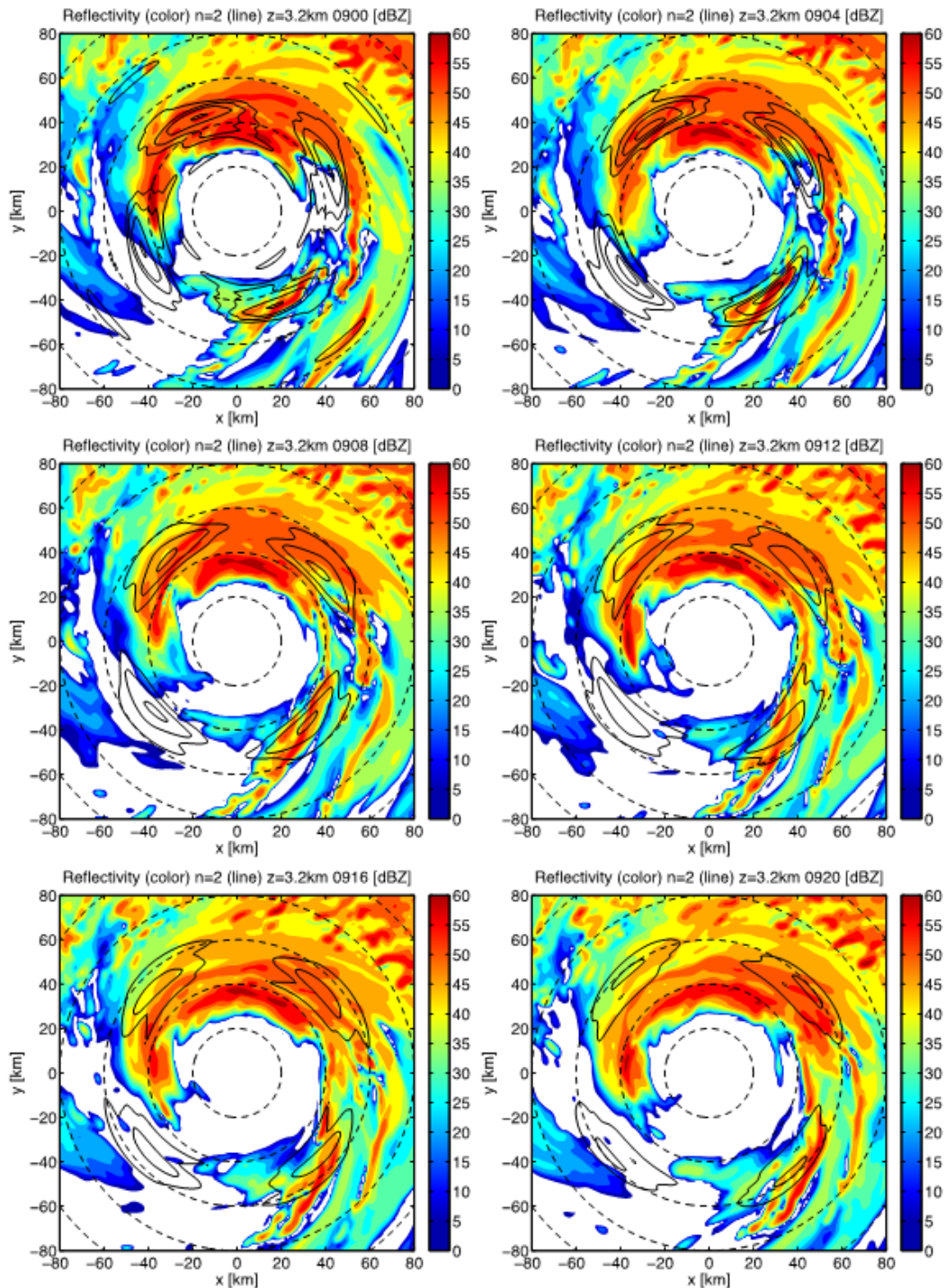


Figure 18. Horizontal cross sections at $z = 3.2$ km of reflectivity every 4 minutes between 0900 UTC and 0920 UTC of August 20, with positive and negative parts of its $n = 2$ component shown as thick and thin solid black lines, respectively. Only $\pm 10, 15, 20,$ and 25 dBZ lines are shown. Dashed concentric circles are for every 20 km. Originally presented as Figure 4 of Part II (Moon and Nolan 2014b).

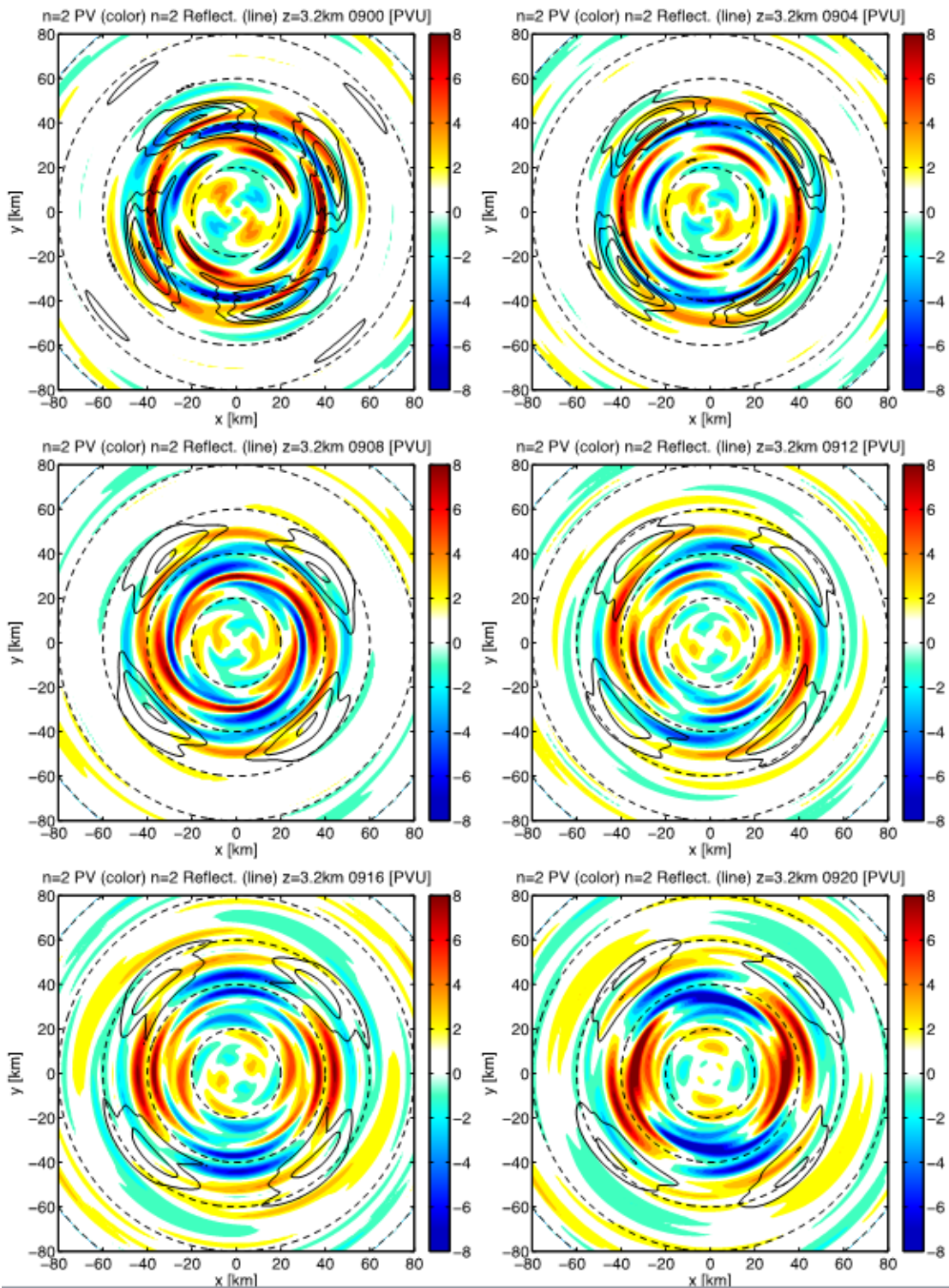


Figure 19. Horizontal cross sections at $z = 3.2$ km of $n = 2$ PV every 4 minutes between 0900 UTC and 0920 UTC of August 20, with overlaid thick and thin solid black lines showing positive and negative parts of $n = 2$ reflectivity as in Figure 18, respectively. Only $\pm 10, 15, 20,$ and 25 dBZ lines are shown. Dashed concentric circles are for every 20 km. Originally presented as Figure 7 of Part II (Moon and Nolan 2014b).

In addition, this paper examined the intrinsic propagation of inner rainbands by comparing the absolute parts (or magnitudes) of the $n = 2$ decomposition coefficients of reflectivity and PV, as done in MK97 (see their Figure 11). However, there were no coherent PV signals associated with the radially outward propagating reflectivity features (see Figures 9, 11-14 of Part II).

An alternative hypothesis was offered by using a simple two-dimensional tracer equation (Equation 2 of Part II). A circular tracer was initially placed in the upshear region and was advected by using the 2-hour average of the depth-averaged horizontal winds between $z = 0.5\text{-}2.0$ km (see Figure 19a of Part II), because inner rainbands were shallow convective features. Figure 20 shows the time evolution of this tracer every 5 minutes. It showed that this tracer moved radially outward and also into the cyclonic direction over time, like many inner rainbands discussed in this paper and previous studies. The radial outward movement was due to the low-level radial outflow in the upshear region that developed in response to the presence of environmental vertical wind shear. At the same time, the deformation field associated with the mean horizontal wind field (see Figure 19b of Part II) turned the initially circular tracer into spiral shapes. Based on the results, Part II argued that inner rainbands propagated radially outward with time because convective features (and hydrometeors associated with them) generated in the upshear region were simply advected by the swirling mean horizontal wind field while being deformed into spiral shapes by its deformation field. **(MOON).**

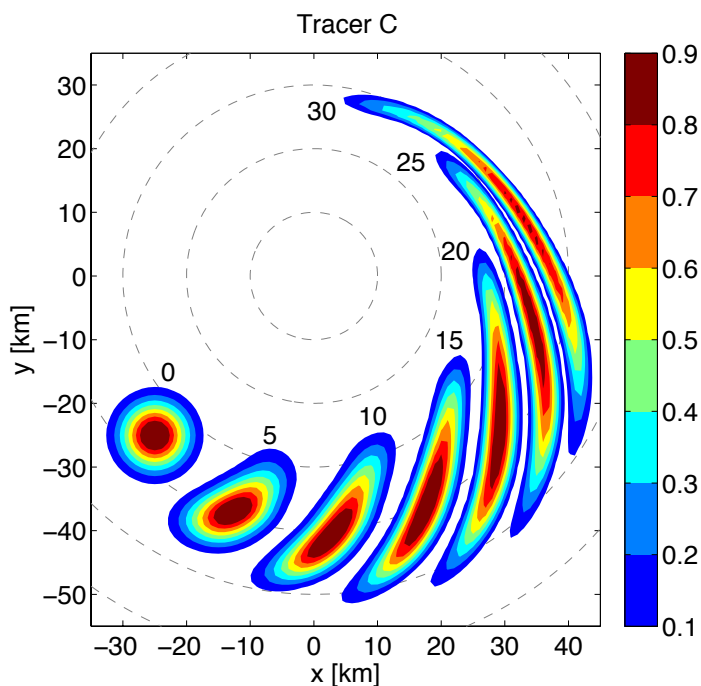


Figure 20. Time evolution of a tracer every 5 minutes in a simple two-dimensional tracer equation (Equation 2 of Part II). Dashed concentric circles are for every 10 km. The tracer C at $t = 0$ minute has a Gaussian bubble-like structure (Equation 3 of Part II), centred at $x = -25$ km and $y = -25$ km. Originally presented as Figure 20 of Part II (Moon and Nolan 2014b).

4.1.7 Terrain Impacts on TC structure

(YING) Taiwan Island is frequently affected by TCs over the western North Pacific. Meanwhile, the island usually exerts a significant influence on TC structure change when it approaches the mountainous area. Recent studies find that the impact Taiwan Island has on TC structure change depends on the approach angle of the TC.

Statistical analysis from Hu et al. (2012) indicated that the structure of TCs change remarkably when they made landfall from the east side of Taiwan Island. The radii of force 8 and 10 wind circles of TCs clearly decrease after landfall, while the radius of maximum wind speed increases gradually. Some TCs have a hollow structure with large areas of less cloud and weak wind in typhoon core region. Based on wind profiler observations, Pan et al. (2010) found that typhoons could be split into upper and lower parts when they passed the leeward side of the Central Mountain Range on Taiwan Island.

For TCs passing Taiwan Island in the north-south direction, the structure change is different. Hu et al. (2013) found that the cloud system shape of Typhoon Nari (0116) evolved from circular to semicircular when it crossed Taiwan Island from north to south (Figure 21). Analysis indicates that Taiwan topography intensified the windward lifting over the Taiwan Strait and restrained the ascending motion on the lee side over the ocean east to Taiwan. At the same time, the channel effect of Taiwan Strait may strengthen the low-level jet in Nari's western periphery, which also enhances convection. However, for Typhoon Meranti (1010), which approached Taiwan Island and entered Taiwan Strait from south to north, the topography effect resulted in a different structure change. Numerical sensitivity experiments demonstrate that mesoscale vortexes can be induced over Taiwan Strait due to the topography when Meranti entered the strait, resulting in a wave that enhanced convection (YING).

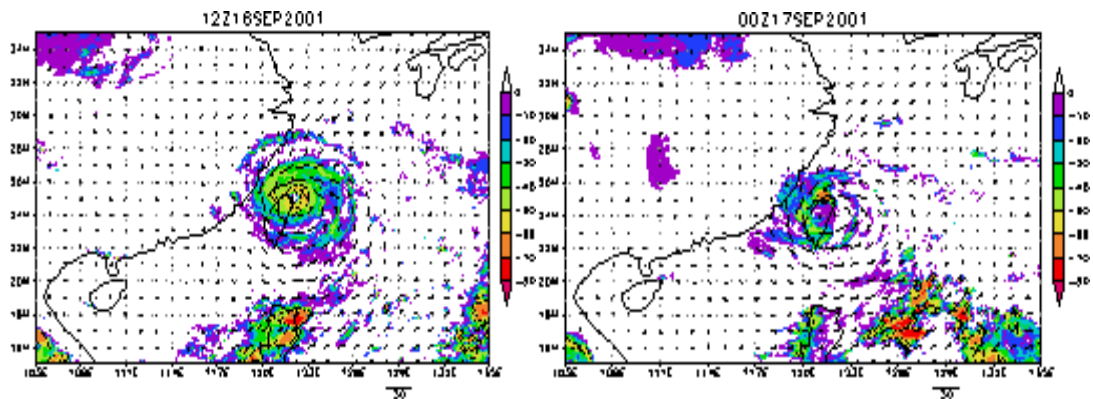


Figure 21. Model-simulated Bright-Body Temperature (TBB) (shaded, °C) and 850 hPa wind vectors (ms^{-1}) before (left) and after (right) landfall

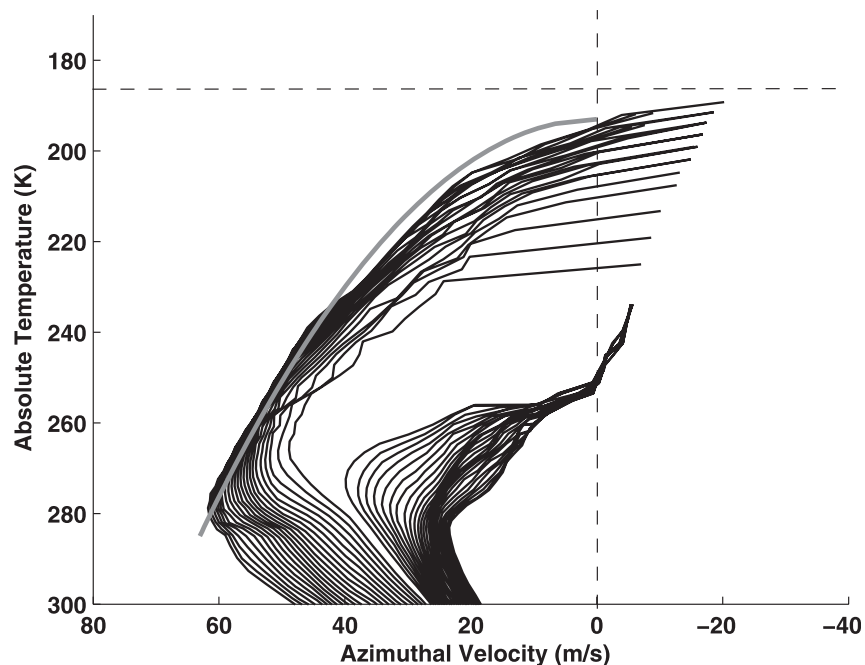


Figure 22. Family of surfaces (thin black curves) of constant absolute angular momentum traced versus absolute temperature and azimuthal velocity. The thick gray curve shows the shape of the angular momentum intersecting the boundary layer top at the radius of maximum winds, calculated assuming thermal wind balance. The dashed vertical line represents vanishing azimuthal wind, while the dashed horizontal line shows the ambient tropopause temperature. The innermost angular momentum surface originates near the radius of maximum wind. (From Emanuel and Rotunno 2011)

4.1.8 TC outflow and relationship to radial structure

(CHAVAS) Emanuel and Rotunno (2011; ER11) derive a theoretical solution for the radial structure of the gradient wind at the top of the boundary layer that is valid in the ascending region of the storm. The solution links the radial distribution of angular momentum at the top of the boundary layer to the stratification of the outflow aloft (Figure 22). The stratification is set by small-scale turbulence in the upper troposphere generated by the Kelvin-Helmholtz instability of the outflow itself; in this way it is termed "self-stratifying". This turbulence will act to restore the flow rapidly toward marginal criticality, such that the Richardson number is at or near the critical value for the onset of turbulence. Positing that the TC vortex is subcritical, information (waves) may propagate inwards against the outflow. Therefore, because convection closely follows a moist isentrope, vertical stratification of the outflow equates to a radial gradient in convective outflow temperature, such that the outflow temperature INCREASES with radius for radii beyond RMW. Following from classical potential intensity theory, an INCREASE in outflow temperature with radius translates to a decrease in the gradient wind speed with radius at the top of the boundary layer. The solution is a function of the ratio of surface exchange coefficients of enthalpy and momentum and takes as free parameters storm intensity (V_{max}) and either the radius of maximum winds or the outer radius where the wind vanishes ER11 compares this solution to output from an axisymmetric numerical model and demonstrate that it is able to credibly replicate the inner-core wind structure for typical estimates of the ratio of exchange coefficients in nature (Figure 23) (CHAVAS).

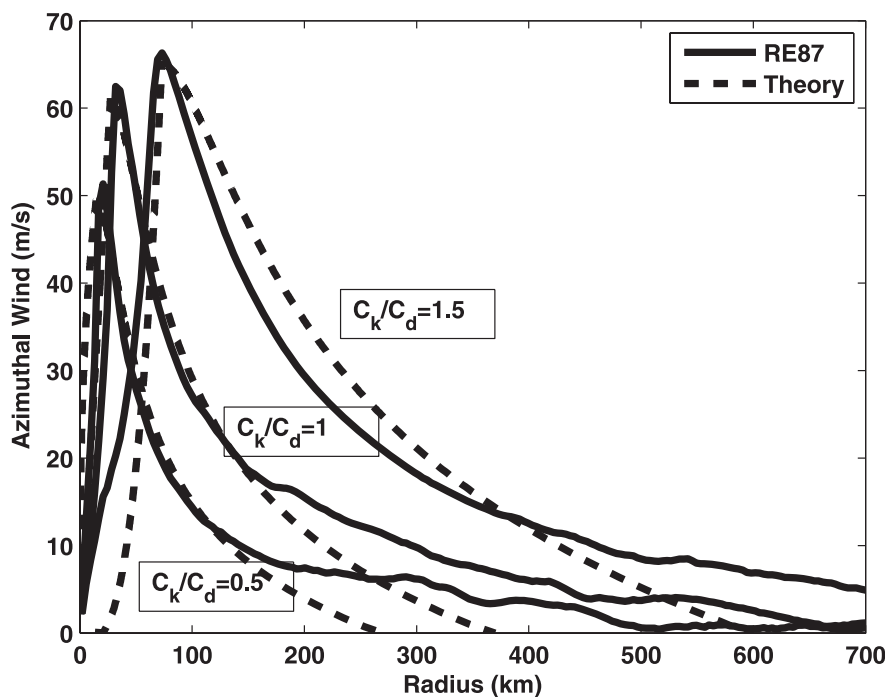


Figure 23. Solutions of the theoretical model compared to the radial profiles of azimuthal wind 12 grid points above the surface, averaged over the last 24 h of three simulations using an updated version of the Rotunno and Emanuel (1987) numerical model (solid). The three pairs of curves correspond to three different ratios of the surface exchange coefficients. (From Emanuel and Rotunno 2011)

4.1.9 TC size, size change, and new size/structure climatologies

(STOVERN) Stovern and Ritchie (2012) conducted a series of sensitivity simulations with the WRF-ARW forecasting model in order to study how the initial vertical atmospheric temperature profile can impact TC size and structure changes. They found that decreasing the atmospheric temperature, while keeping the SST and relative humidity constant, allows for an overall larger TC to form in terms of both the wind and precipitation fields (e.g. Figure 24). Conversely, warming the initial atmospheric temperature leads to a smaller TC wind field with a smaller, yet more intense core of precipitation.

The mechanisms for forming a larger TC in the cool simulations (i.e. C1-C3) are related to the amount of surface energy fluxes within the TC and its surrounding environment. Cooling the atmospheric temperature increases the latent and sensible heat fluxes across the entire computation domain which initially causes the TC to form with a larger area of radial inflow, driven by a larger-forming convective field. Figure 25a shows the radial wind circulation and vertical velocities for the coldest simulations in the set, C3.

In the warm atmosphere cases (i.e. W1-W3), the initial CAPE and specific humidity profile is initially higher which causes the TC to rapidly intensify with a tighter wind field and a stronger, more compact precipitation field but with a reduced area of radial inflow (Figure 25b). Once the CAPE and moisture is depleted through convective processes in the warm simulations, the surface energy fluxes are not high enough to recharge the boundary layer with heat and moisture so convection weakens, the intensity decreases, and the TCs remain compact. The physical mechanisms that are identified relating to the different size and structure of each simulation are consistent with the results obtained in Xu and Wang (2010a, b) and Hill and Lackmann (2009).

(STOVERN)

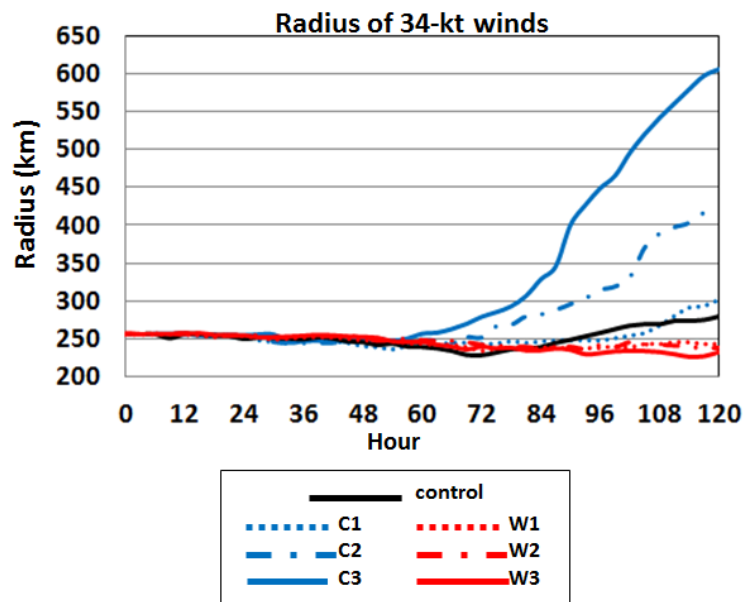


Figure 24. Time evolution of the radius of 34-kt winds (i.e. size) for seven temperature sensitivity simulations performed on an f-plane. Simulations cooler (warmer) than the control (in 1° C increments) are represented with blue (red) lines.

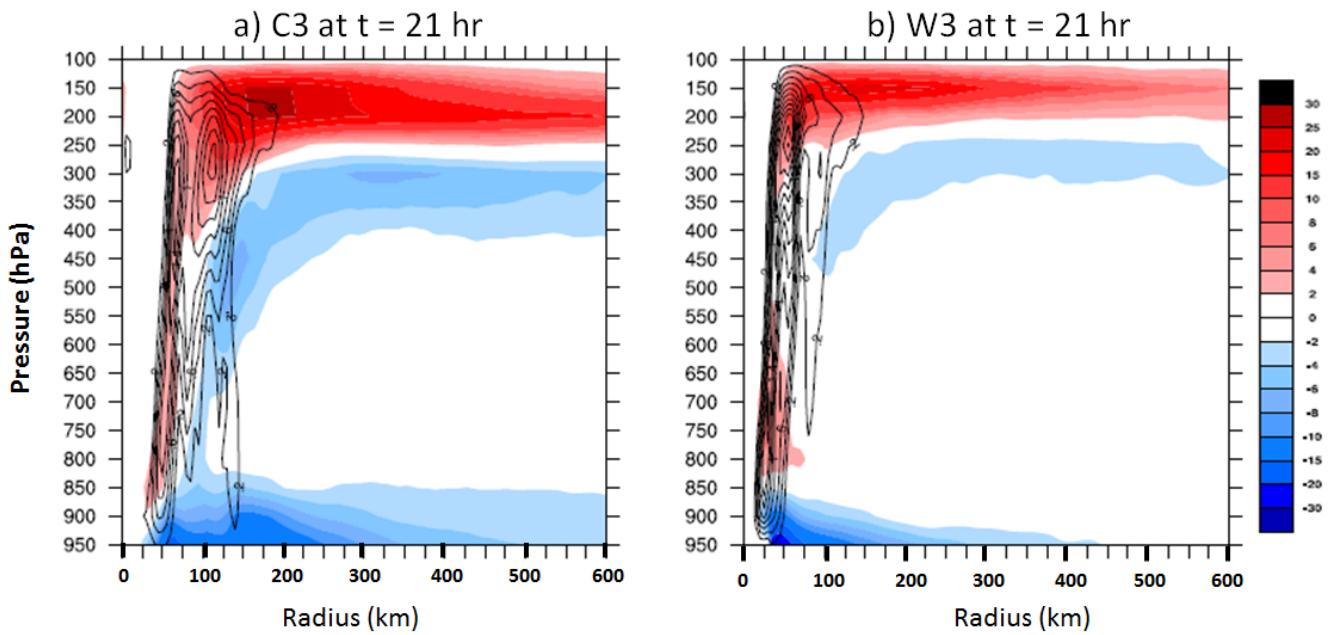


Figure 25. Vertical wind velocities (contour increment is 0.2 m/s) overlaid with radial wind velocities. Blue shading represents radial inflow and red shading represents outflow (m/s) at $t = 21$ hr for simulations a) C3 and b) W3.

(**CHAVAS**) Chavas and Emanuel (2010) focuses on the characterization and variability of the size and radial structure of the low-level wind field of a tropical cyclone. A QuikSCAT surface wind vector database was used to develop a climatology of tropical cyclone size as measured by the radius of 12 m/s (r_{12}), from which the outer radius of vanishing winds (r_0) was estimated using an analytical outer wind structure model. Size was found to be log-normally distributed globally, spanning a wide range of values (Figure 26); however, its variability was largely uncorrelated with various environmental variables (e.g. potential intensity, Coriolis parameter) or aspects of the inner core structure (storm intensity), reflecting past observations of the independent variability of the inner and outer structure of the storm.

Seeking a more fundamental understanding of size and structure, Chavas and Emanuel (2014) explored these properties in a tropical cyclone at statistical equilibrium in an axisymmetric model. The model environment was set up to reduce the complexity of the system to enable as simple and direct an analysis of tropical cyclone dynamics as possible, allowing for a comprehensive evaluation of the physical parameters that modulate storm size and structure. This work demonstrated that, at equilibrium, the size of the outer circulation of a tropical cyclone scales with the theoretical length scale given by the ratio of the potential intensity to the Coriolis parameter, V_p/f . Furthermore, the complete radial wind structure is determined principally by a single non-dimensional parameter given by the ratio of the storm length scale (V_p/f) to the parameterized eddy radial mixing length scale (Figure 27). The structure of the entire outer wind field beyond the inner core is readily captured by the analytical outer wind structure model employed in the aforementioned observational study. Finally, in contrast to the size and structure of the storm's outer circulation, the inner-core structure (V_{max} , r_{max}) is strongly modulated by the radial mixing length, again reflecting the observation that inner and outer structure of observed storms covary only minimally.

However, the equilibration timescale is on the order of tens of days, while real storms in nature often do not last this long and in any case exist in a thermodynamic environment that continuously changes in time. As a result, the length scale V_p / f does not explain the variability of storm size in nature. (**CHAVAS**).

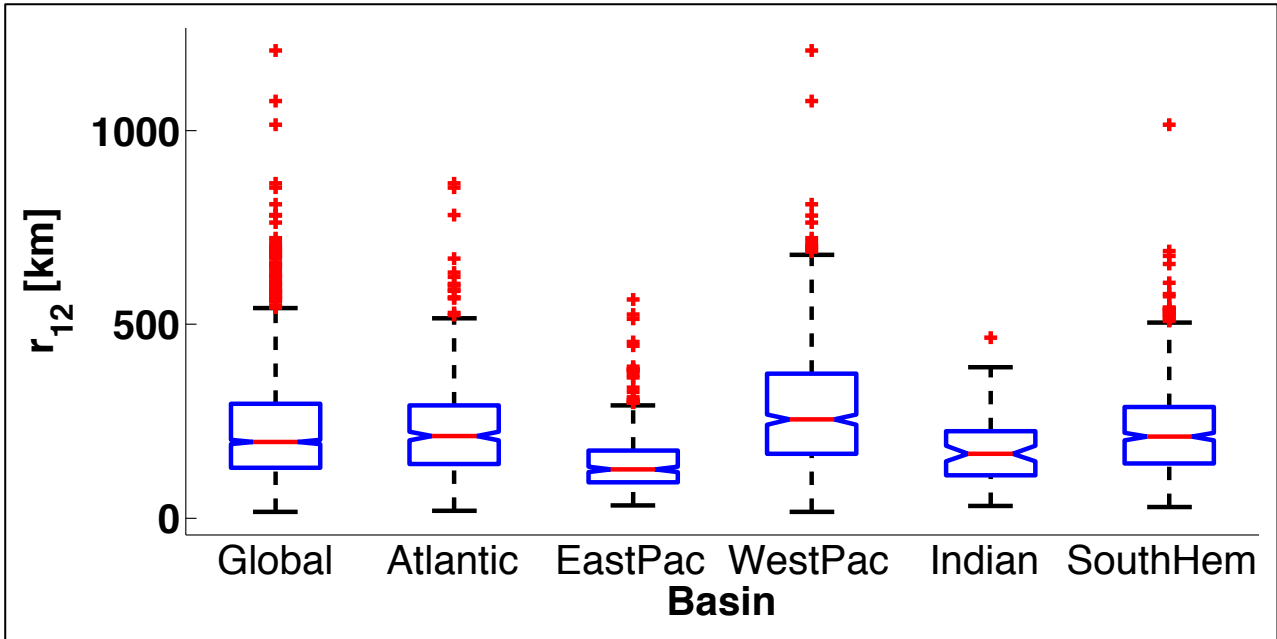


Figure 26. Box-and-whisker plot of r_{12} distribution globally and across basins. Adapted from Chavas and Emanuel (2010)

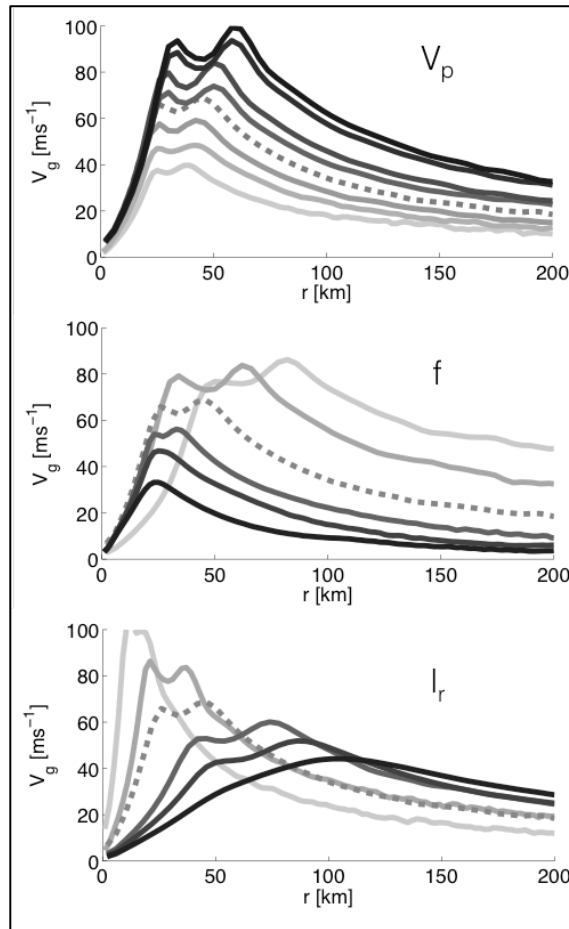


Figure 27. Equilibrium radial gradient wind profiles for variable V_p , f , and l_r (radial mixing length); darker shades indicate larger parameter magnitude. Adapted from Chavas and Emanuel (2014)

(KNAFF) In seeking to produce an objective climatology of TC size, Knaff et al. (2014) compared storm-centred infrared (IR) imagery of TCs to the 850-hPa mean tangential wind at a radius of 500km calculated from 6-hourly global numerical analyses for North Atlantic and eastern North Pacific TCs for the period 1995–2011. V500 estimates were scaled using the climatological vortex decay rate beyond 500km to estimate the radius of 5 kt winds (R5) or TC size. A much larger historical record of TC-centred IR imagery (1978–2011) was then used to estimate TC sizes and form a global TC size climatology. Many of the findings of this study reconfirm past work in the North Atlantic and western North Pacific but have put these in a global context (Figures 28 and 29). Results confirm that the propensity for large TCs increases when TCs form during seasons that are characterized by enhanced low-level vorticity and when TCs move into environments characterized as increasingly baroclinic, especially after peaking in intensity and prior to recurvature. This study confirms larger major hurricanes occur in the western North Pacific, which agrees with consensus. As others have shown, small TCs tend to form during seasons when low-level vorticity is provided by the incipient disturbance rather than the synoptic environment. In those cases the flow is often characterized by easterly trade winds or being located in the centre of the subtropical ridge (as is often the case with midget typhoons). Post-peak intensity TC growth can also be halted by landfall and other rapid weakening. However, a few new findings result from this study. Composites of the IR imagery indicate the average eye sizes are similar for small-, average-, and large-sized major hurricanes. In a global sense, there is a clear indication that small major hurricanes predominate at low latitudes. This study also allows for the direct comparison of size distributions between the individual TC basins and the identification of the smallest and largest major hurricanes in each of these basins. These summaries clearly show the differences between basins and confirm previous findings that the eastern North Pacific produces TCs that are about 2/3 the size of other basins. We also find that there are preferred regions, seasons, and track types for TC sizes and growth tendencies. Information about the life cycle of TC growth with respect to the timing of maximum intensity is provided and leads to these findings:

- 1) TCs tend to grow more as they intensify.
- 2) If a TC is relatively large (small) in its formative stages, it likely will be relatively large (small) when it reaches maximum intensity.
- 3) Different basins display both markedly different initial sizes and life cycle size evolutions.
- 4) On average TCs shrink after peak intensity, save for in the North Atlantic.
- 5) The average North Atlantic major or minor hurricane maintains its size after peak intensity and stronger TCs continue to grow after peak intensity (suggesting results obtained from the Atlantic are not applicable everywhere) **(KNAFF)**.

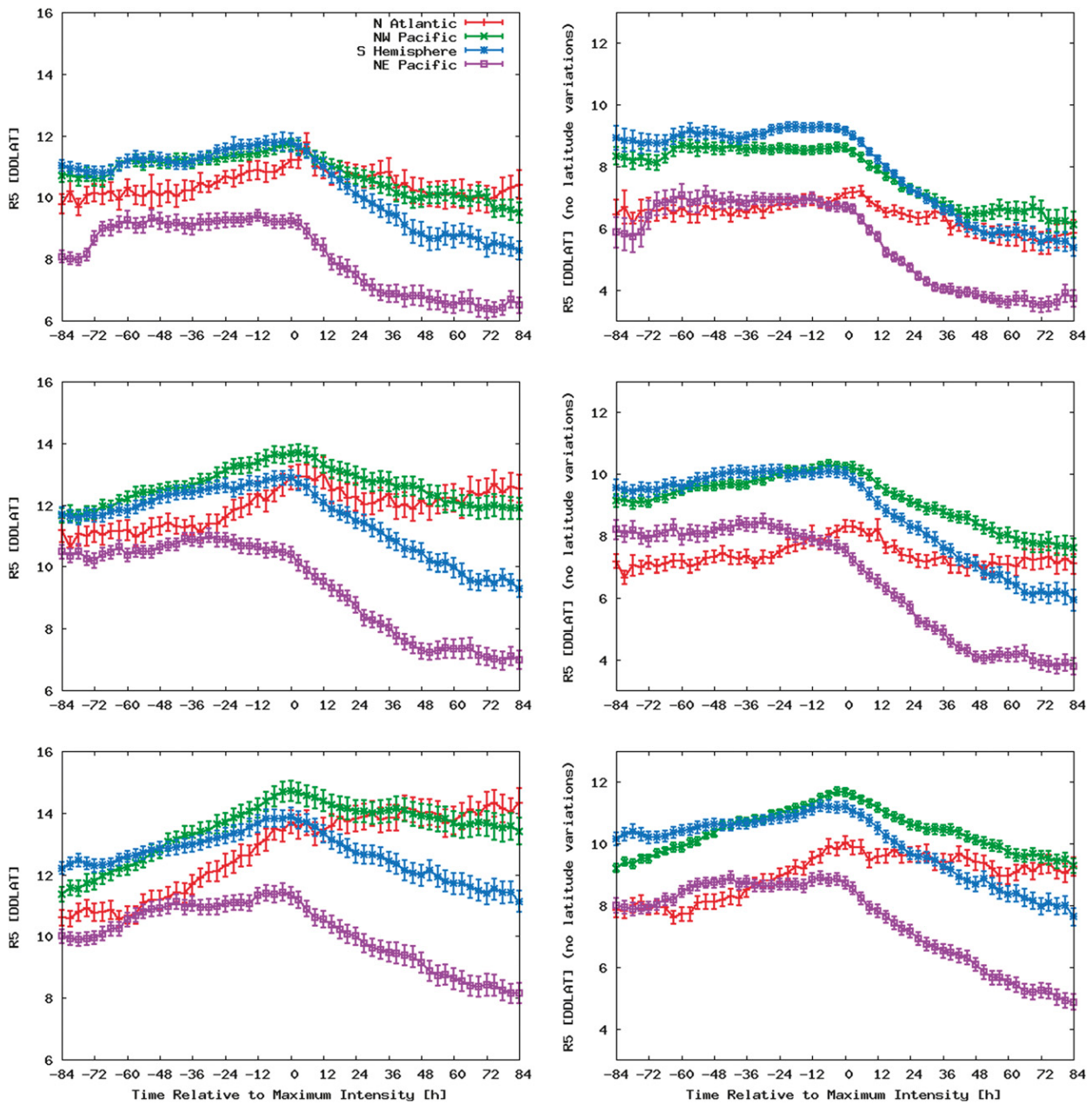


Figure 28. (Figure 5 from Knaff et al. 2014). Composites of TC size (R5) based on the timing of maximum intensity (i.e., time 5 0 h): for TCs in the intensity V_{max} ranges (top) $34 \leq V_{max} \leq 64$ kt, (middle) $64 \text{ kt} \leq V_{max} \leq 96$ kt, and (bottom) $V_{max} \geq 96$ kt of (left) R5 (right) R5 calculated without the latitude contribution. Vertical bars provide the standard error associated with each 3-hourly mean R5 value. The R5 units are in DDLAT.

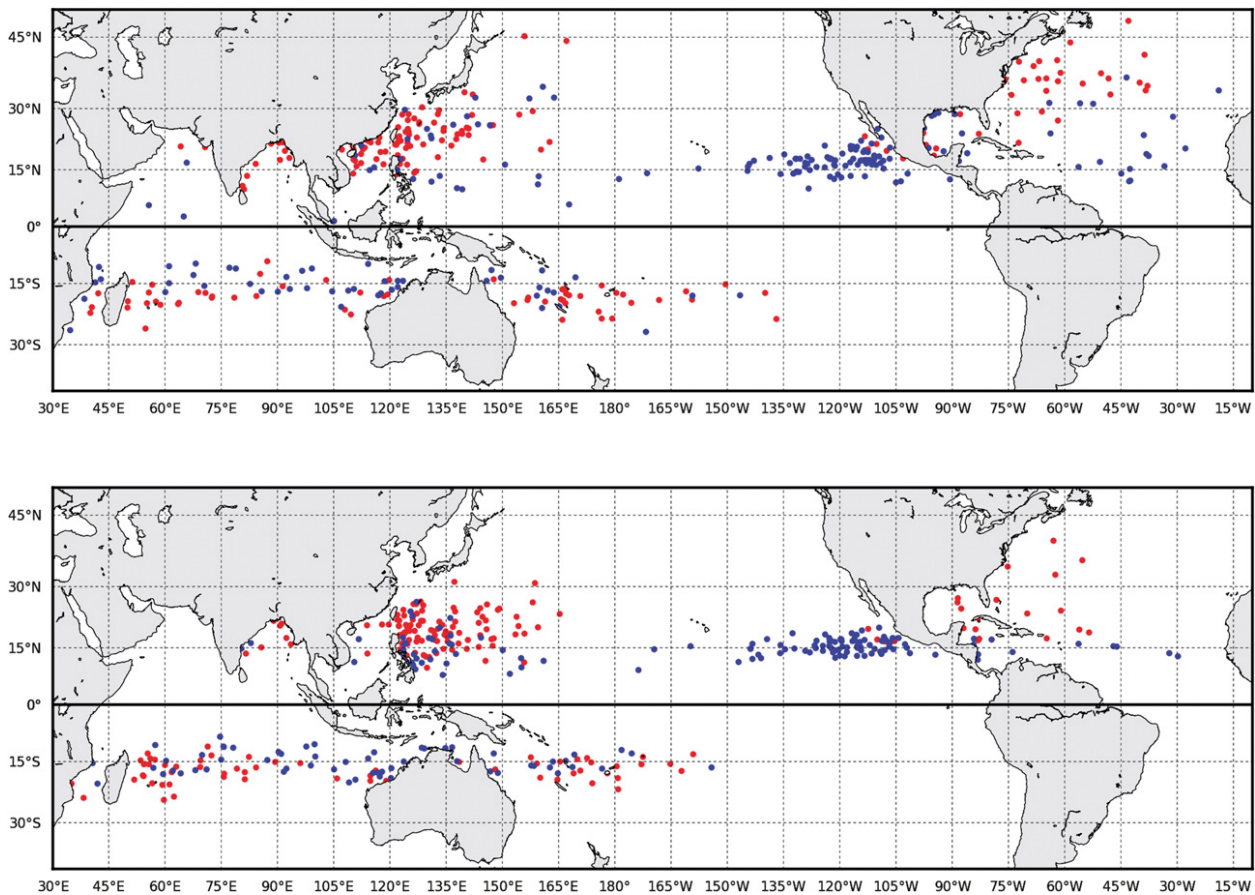


Figure 29. (Figure 6 from Knaff et al. 2014). Locations of the largest (red) and smallest (blue) 25% of TCs based according to R5. (top) TCs that reached minor hurricane intensity and (bottom) TCs that reached major hurricane intensity. Locations are based on the first maximum lifetime intensity.

(VIGH) Musgrave et al. (2013) conduct a theoretical exploration of the life cycle of TC. Observations and simple numerical models suggest that the typical TC lifecycle consists of an *incipient stage*, with slow intensification up to about 25 ms⁻¹, a *deepening stage*, in which the TC both intensifies and grows in size more rapidly up to about 60 ms⁻¹, and finally, a *mature stage*, in which the TC's intensity is more or less steady but the size continues to grow. The TC lifecycle trajectory can be viewed as a trajectory through a phase space that consists of maximum intensity (Vmax) and integrated kinetic energy (K). Figure 30 shows the typical TC life cycle, starting from the lower left corner (incipient stage), sloping upward to the right (deepening stage), and the reaching an apex at peak intensity and curving back and up to the left (mature stage). Concentric eyewall cycles represent a deviation from this typical curve with a temporary weakening in Vmax while the size continues to grow. Additionally analogies are drawn to the main sequence of stellar evolution.

To theoretically explore the possible reasons behind this typical TC life cycle, the authors use the balanced vortex model to solve for the geopotential tendency equation. From this, they pose the boundary layer problem that relates the diabatic heating, the Rossby length, and the radial distribution of the mass field (which can be expressed as the tangential wind tendency or temperature tendency). Solving numerically, they explore the resulting temperature tendency and tangential wind tendencies that result from a Gaussian wind profile in the presence of an annular ring of diabatic heating profile that represents the heating in the eyewall of a TC. They examine the sensitivity of these results to different heating profiles meant to illustrate typical TCs from categories 1-5 with varying RMW, and profiles with different profile shapes including vortex skirts.

Their results corroborate previous work that showed that a crucial factor in the rapid intensification of TCs is the presence of diabatic heating in the presence of a small Rossby length. Their numerical results show that rapid intensification will not occur unless at least some deep convection occurs well within the vortex skirt of the vortex. Thus, the vortex intensification rate is an inherently difficult problem, since it depends not on the bulk or average vorticity and heating in the inner core, but critically on the radial distribution of these. (VIGH)

(COSSUTH) Prior to the climatology of eye formation previously discussed by Vigh et al. (2012), climatologies of structure using in-situ observations were performed by Merrill (1984), Weatherford and Gray (1988ab) Kimball and Mulekar (2004), Piech (2007), Murray (2009), Musgrave (2011), and Musgrave et al. (2012). Since the last IWTC, recent work by Musgrave (2011) began with a similar methodology to Kimball and Mulekar (2004) and Piech (2007) by using VDMs to show the distribution of eye size within the Atlantic basin by intensity and storm age. Musgrave (2011) then related the location of diabatic heating in a balanced vortex model to changes in Integrated Kinetic Energy (IKE) and maximum sustained wind (V_{max}). This work is expanded upon in Musgrave et al. (2012) to demonstrate that a TC's intensity and size changes are both dependent on the vorticity and diabatic heating profiles in the inner-core. Cossuth et al. (2014) also builds upon these analyzes by using VDM and ATCF (Sampson and Schrader 2000) data to aggregate and intercompare characteristics of inner-core evolution by an intensity and core size phase diagram. Distributions of eye and core size counts as well as thermodynamic and dynamic parameters in Cossuth et al. (2014) demonstrate additional dimensionality in depicting TC evolution.

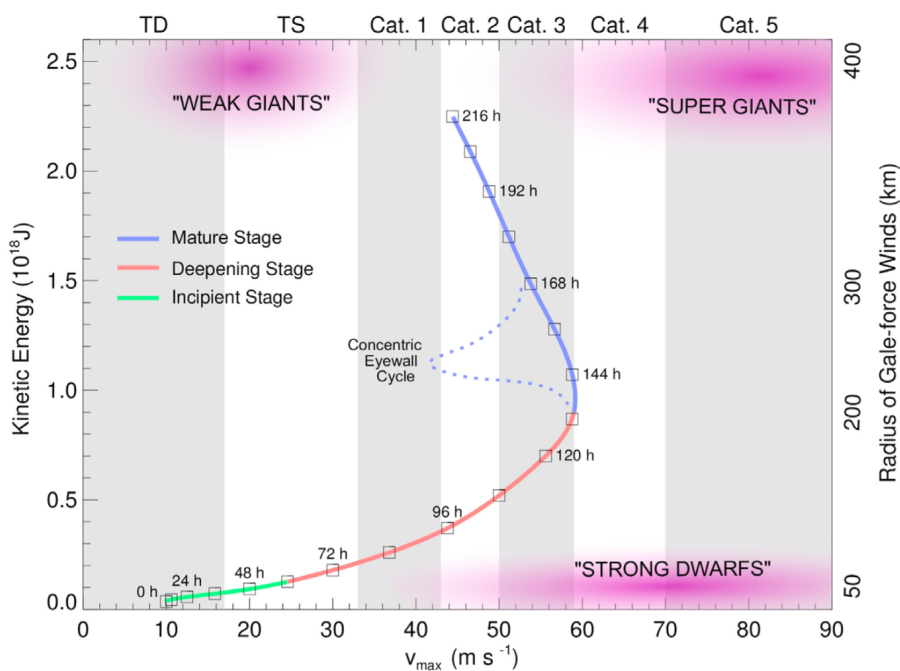


Figure 30. (from Musgrave et al. 2013): The multi-coloured curve shows the K-Vmax time evolution of a typical TC. The incipient, deepening, and mature stages are indicated respectively by green, red, and blue. Time marks are every 12 h. Labels across the top of the figure stand for tropical depression (TD), tropical storm (TS), and the five Saffir-Simpson categories. Excursions off this “main sequence” can be caused by PV mixing and ERC. Three other types of time evolution occur in small, intense storms labelled here as “Strong Dwarfs,” in large, mature storms labelled here as “Super Giants,” and in large tropical depressions or tropical storms that never reach hurricane intensity, labelled here as “Weak Giants.” For rough quantitative interpretation, the ordinate is also labelled (on the right) in terms of the radius of gale-force winds.

A multi-decadal climatology of TCs as observed by multiple passive microwave imagers was gathered and standardized in Cossuth (2014) and Cossuth et al. (2015). Using this data, structural metrics similar to those observed by aircraft and quantified in Piech (2007), Murray (2009), Vigh et al. (2012), and Cossuth et al. (2014) were calculated and composited to directly compare and contrast the ability for microwave data to replicate and augment aircraft structural measures. This digital microwave imagery builds upon a previous climatology (Knapp 2008) by compiling multiple sensors and standardizing the output. The ice scattering channels of 85, 89, and 91 GHz were recalibrated to 89 GHz using empirically derived coefficients by Yang et al. (2014). Further, SSM/I and SSMIS data were optimally interpolated via the Backus-Gilbert technique (Poe 1990) using weighting factors determined by the sensor characteristics. Finally, TCs were analyzed and recentered with the ARCHER technique (Wimmers et al. 2010) (example given in Figure 31a).

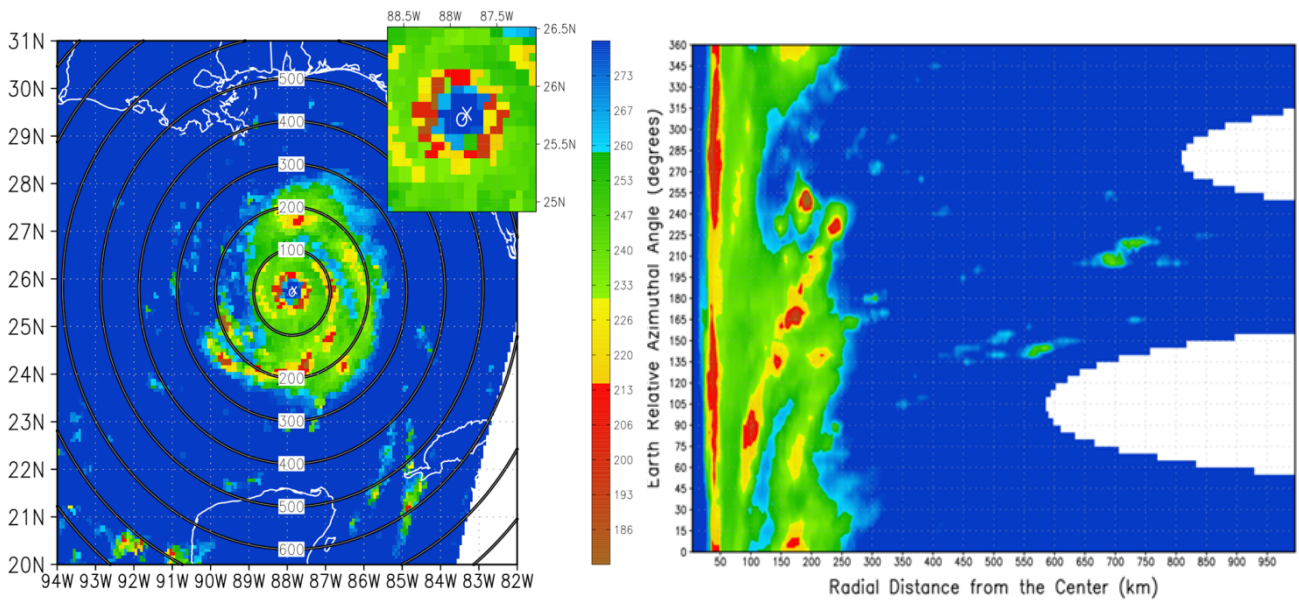


Figure 31. a) 85GHz PCT image of Hurricane Katrina on August 28, 2005, 1244 UTC. Retrieved from HURSAT and measured by the DMSP-F13 SSM/I. Inset in the upper right zooms in on the ARCHER derived position ('O') and the interpolated best track ('X'), which are offset by roughly 1/10 of a degree. b) Transformation of (a) into polar coordinates, with (a) analyzed from the ARCHER derived centre ('O').

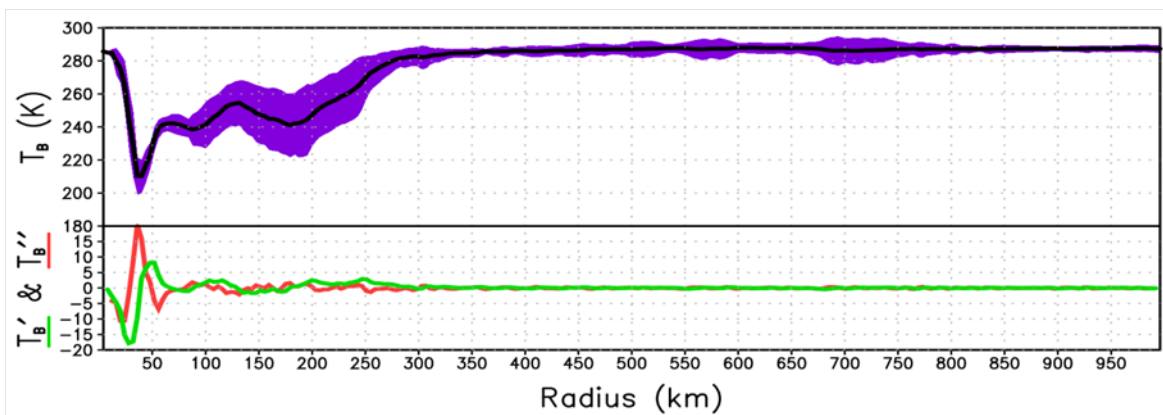


Figure 32. Azimuthal average brightness temperature of Figure 31 in black, with the standard deviation shaded about the line in purple. The first (green) and second (red) derivatives of the azimuthal average are shown below that. The inflection point noted in the second panel is what was used as for core size.

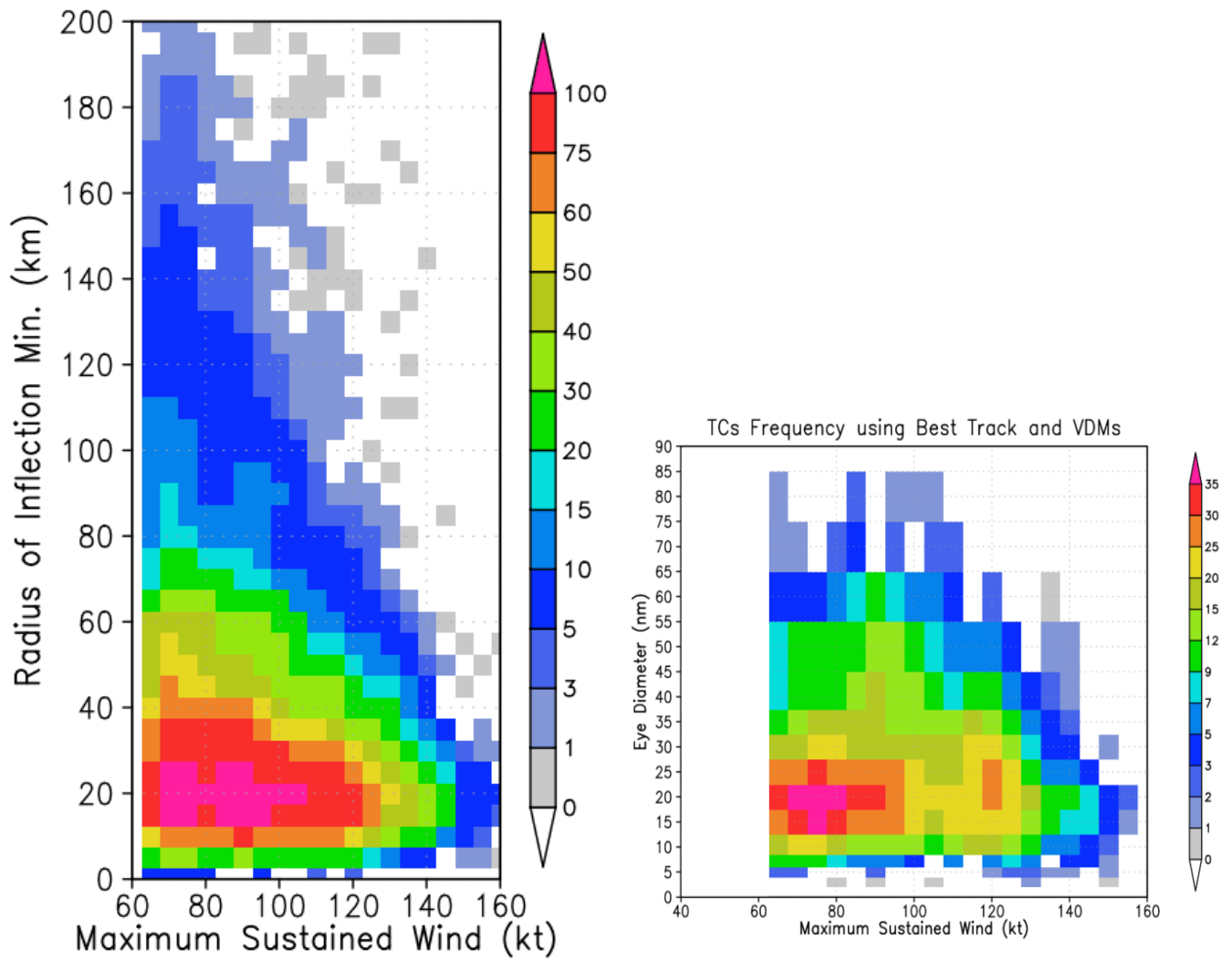


Figure 33. Left) Existence diagram of combinations of core size (as measured by inflection point radius) and maximum sustained wind. Right) The vortex data message existence based upon reconnaissance vortex message data for the Atlantic basin. The two figures are positioned such that they can be intercompared based upon both axes.

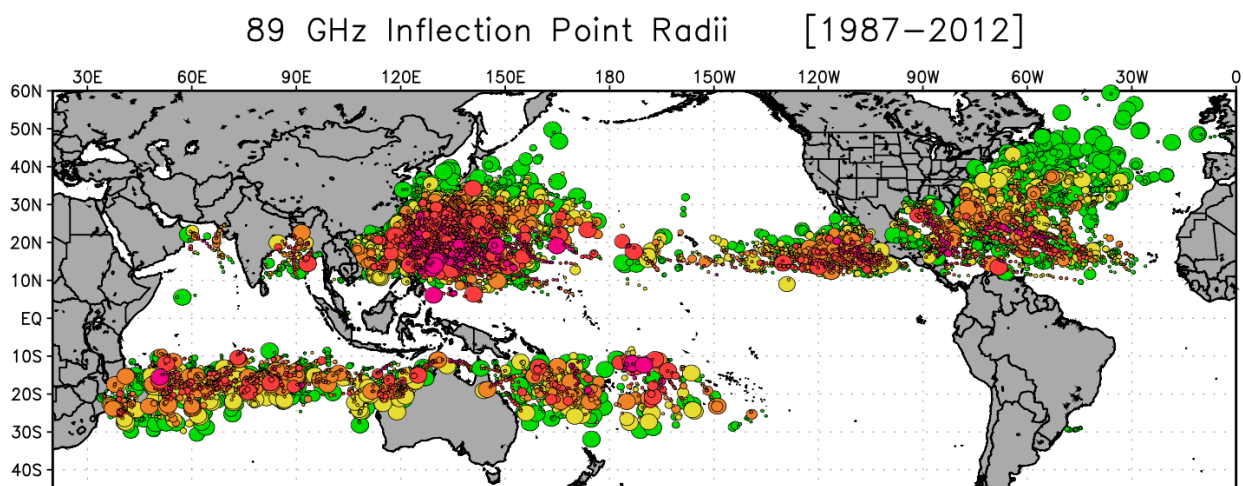


Figure 34. Global climatology of TC size as measured by the inflection point radius using HURSAT 89 Ghz imagery from 1987-2012 from Cossuth (2014)

Coordinate transformation to polar coordinates is shown in Figure 31b, azimuthal averaging of the brightness temperature is shown in Figure 31a, with the first and second radial derivatives of that azimuthal average shown in Figure 31b. The inflection point – global minimum of the first derivative in Figure 32b – is used in Cossuth (2014) as the measure of core size. With that objective measure of core size, an existence climatology of core size was performed on the entire 89GHz passive microwave database in Cossuth et al. (2015). This climatology is presented in Figure 33a and is compared to the VDM-based climatology from Cossuth et al. (2014) in Figure 33b. A global spatial climatology of TC size using this metric is shown in Figure 34. This represents the preliminary steps in the first objectively based TC core size climatology using remotely sensed data (**COSSUTH**).

(**RAMA RAO**) Mohapatra and Monica (2014) have analyzed the mean characteristics of surface wind distribution and hence the structure of TCs for RSMC, New Delhi operational requirement based on the real time data available from CIRA during 2007-2013. The database comprised of 25 TCs over the North Indian Ocean (NIO) consists of 19 TCs over the Bay of Bengal (BOB) and 6 TCs over the Arabian Sea (AS). The analysis of TC size in that study indicates that the average size of TCs (radius of 34 kts wind) over the AS varies from 43 to 72 nm in cases of Cyclonic Storm (CS) and Severe Cyclonic Storm (SCS), respectively, during pre-monsoon season and 70 nm for both CS and SCS during post monsoon season. Similarly, the average size of TCs over the BOB is about 73 to 107 nm in cases of CS, SCS and Very SCS, respectively, during pre-monsoon season and 57 to 102 nm during post monsoon season. The average size of the CS over the BOB is higher than that over the AS during pre-monsoon season and there is no significant difference during post-monsoon season (**RAMA RAO**).

4.1.10 Summary and recommendations

Since the last IWTC conference there have been considerable research advances on the various aspects of TC structure, structure change, and the processes involved therein. Several prior theories on structure change, including eye formation and eyewall replacement cycles, have been re-examined. Considerable research has been presented on the formation and evolution of TC spiral bands. Further, several new climatologies have been developed, including: eye formation stage, measures of TC size, and measures of TC inner core size. The relationships among TC eyewall tilt, TC intensity and TC intensity change have been aggressively explored with new insights found. Nonetheless, it is clear that there remain many unanswered questions in this operationally and theoretically important area – with numerical models not yet agreeing sufficiently with observational studies (e.g. HFIP SRC reports 2013 and 2014: Nolan et al. 2013; Hart et al. 2014). The WG strongly encourages further research in the coming years within the broad areas of TC Structure Change and Structure Change Processes. As a final recommendation, it is clear based upon the breadth and depth of the research in this report (and, thus, its length), that this WG scope should be split into two for future IWTC meetings – perhaps into inner core and outer structure.

4.1.11 References

- Abarca, S. F. and M. T. Montgomery, **2013**: Essential dynamics of secondary eyewall formation. *J. Atmos. Sci.*, 70, 3216–3230.
- Abarca, S. F. and M. T. Montgomery, **2014**: Departures from axisymmetric gradient wind balance during secondary eyewall formation. Accepted. *J. Atmos. Sci.*
- Abarca, S. F., and K. L. Corbosiero, **2011**: Secondary eyewall formation in WRF simulations of Hurricanes Rita and Katrina (2005). *Geophys. Res. Lett.*, 38, L07802, doi:10.1029/2011GL047015.

- Akter, N., K. Tsuboki, **2012**: Numerical Simulation of Cyclone Sidr Using a Cloud-Resolving Model: Characteristics and Formation Process of an Outer Rainband. *Mon. Wea. Rev.*, 140, 789–810. doi: <http://dx.doi.org/10.1175/2011MWR3643.1>
- Backus, G., and F. Gilbert, **1968**: The resolving power of gross earth data. *Geophys. J. Roy. Astron. Soc.*, 16, 169–205.
- Barnes, G. M., E. J. Zipser, D. Jorgensen, and F. Marks, **1983**: Mesoscale and convective structure of a hurricane rainband. *J. Atmos. Sci.*, 40, 2125–2137.
- Bell, M. M., M. T. Montgomery, and W.-C. Lee, **2012**: An axisymmetric view of concentric eyewall evolution in Hurricane Rita (2005). *J. Atmos. Sci.*, 69, 2414–2432.
- Chavas D. R. and K. A. Emanuel, **2010**: A QuikSCAT climatology of tropical cyclone size, *Geophys. Res. Lett.*, 37, L18816, doi:10.1029/2010GL044558.
- Chavas D. R. and K. A. Emanuel, **2014**: Equilibrium tropical cyclone size in an idealized state of radiative-convective equilibrium. *J. Atmos. Sci.*, 71(5): 1663–1680.
- Chen, H., and D.-L. Zhang, **2013**: On the rapid intensification of Hurricane Wilma (2005). Part II: Convective bursts and the upper-level warm core. *J. Atmos. Sci.*, 70, 146–162.
- Chen, H., D.-L. Zhang, J. Carton, and R. Atlas, **2011**: On the rapid intensification of Hurricane Wilma (2005). Part I: Model prediction and structural changes. *Wea. Forecasting*, 26, 885–901.
- Chen, Y., and M. K. Yau, **2001**: Spiral bands in a simulated hurricane. Part I: Vortex Rossby wave verification. *J. Atmos. Sci.*, 58, 2128–2145.
- Corbosiero, K. L., J. Molinari, A. R. Aiyyer, and M. L. Black, **2006**: The structure and evolution of Hurricane Elena (1985). Part II: Convective asymmetries and evidence for vortex Rossby waves. *Mon. Wea. Rev.*, 134, 3073–3091.
- Cossuth, J. H., R. E. Hart, D. J. Piech, and D. A. Murray, **2014**: The climatological relationship between tropical cyclone intensity and core structure using operational metrics. *Mon. Wea. Rev.*, in revision.
- Cossuth, J. H., **2014**: Exploring a Comparative Climatology of Tropical Cyclone Core Structures. PhD Dissertation, Florida State University, 201 pp.
- Cossuth, J. H., J. Hawkins, S. Yang, K. Richardson, J. Solbrig, M. Surratt, A. Wimmers, and C. Velden, **2015**: Creating a standardized digital climatology of tropical cyclones as observed by passive microwave satellite sensors. *J. Appl. Meteor. Climatol.*, in preparation.
- Das, A.K., Y.V. Rama Rao, V. Tallapragada, Z. Zhang, S.K. Roy Bhowmik, A. Sharma, **2014**: Evaluation of the Hurricane Weather Research and Forecasting (HWRF) model for tropical cyclone forecasts over North Indian Ocean (NIO), *Natural Hazards* (DOI: 10.1007/s11069-014-1362-6).
- DeHart, J., R. A. Houze Jr., and R. Rogers, **2014**: Quadrant distribution of tropical cyclone inner-core kinematics in relation to environmental shear. *J. Atmos. Sci.*, 71, 2713–2732.
- Didlake, A. C., and R. A. Houze, **2009**: Convective-scale downdrafts in the principal rainband of Hurricane Katrina (2005). *Mon. Wea. Rev.*, 137, 3269–3293.
- Didlake, A. C., and R. A. Houze., **2011**: Kinematics of the Secondary Eyewall Observed in Hurricane Rita (2005). *J. Atmos. Sci.*, 68, 1620–1636.
- Didlake, A. C. and R. A. Houze, **2013a**: Convective-scale variations in the inner-core rainbands of a tropical cyclone. *J. Atmos. Sci.*, 70, 504–523.
- Didlake, A. C. and R. A. Houze, **2013b**: Dynamics of the stratiform sector of a tropical cyclone rainband. *J. Atmos. Sci.*, 70, 1891–1911.
- Dolling, K., and G. M. Barnes, **2012**: Warm core formation in Tropical Storm Humberto (2001). *Mon. Wea. Rev.*, 140, 1177–1190.

- Dolling, K., and G. M. Barnes, **2014**: The evolution of Hurricane Humberto (2001). *J. Atmos. Sci.*, 71, 1276–1291.
- Durden, S. L., **2013**: Observed tropical cyclone eye thermal anomaly profiles extending above 300 hPa. *Mon. Wea. Rev.*, 141, 4256–4268.
- Fierro, A. O., R. F. Rogers, F. D. Marks, and D. S. Nolan, **2009**: The impact of horizontal grid spacing on the microphysical and kinematic structures of strong tropical cyclones simulated with the WRF-ARW model. *Mon. Wea. Rev.*, 137, 3717–3743.
- Foerster, A. M., M. M. Bell, S. C. Jones, and P. A. Harr, **2014**: Observations of the eyewall structure of near-extratropical Typhoon Sinlaku (2008) in vertical wind shear. *Mon. Wea. Rev.*, 142, 3372-3392.
- Fudeyasu, H., Y. Wang, **2011**: Balanced Contribution to the Intensification of a Tropical Cyclone Simulated in TCM4: Outer-Core Spinup Process. *J. Atmos. Sci.*, 68, 430–449.
doi: <http://dx.doi.org/10.1175/2010JAS3523.1>
- Gamache, J.F., **1997**: Evaluation of a fully three-dimensional variational Doppler analysis technique.
- Preprints, 28th Conf. on Radar Meteorology, Austin, TX, Amer. Meteor. Soc., 422-423.
- Hart, R. E., D. S. Nolan, J. F. Price, G. M. Barnes, J. Hansen, and W. Schubert, **2014**: 2nd Report of the Scientific Review Committee (SRC) for the Hurricane Forecast Improvement Project (HFIP).
- Hazelton, A.T. and R.E. Hart, **2013**: Hurricane eyewall slope as determined from airborne radar reflectivity data: composites and case studies, *Wea. Forecasting*, 28, 368-386.
- Hazelton, A. T., R. Rogers and R.E. Hart, **2014**: Shear-relative asymmetries in TC eyewall slope, *Mon. Wea. Rev.*, in press.
- Hawkins, J. D., and M. Helveston, **2008**: Tropical cyclone multiple eyewall characteristics. Preprints, 28th Conf. on Hurricanes and Tropical Meteorology. Orlando, FL, Amer. Meteor. Soc., 14B.1.
- Hence, D. A., and R. A. Houze Jr., **2008**: Kinematic structure of convective-scale elements in the rainbands of Hurricanes Katrina and Rita (2005). *J. Geophys. Res.*, 113, D15108.
- Hill, K. A., and G. M. Lackmann, **2009**: Influence of environmental humidity on tropical cyclone size. *Mon. Wea. Rev.*, 137, 3294–3315.
- Holton, J. R., **2004**: An Introduction to Dynamic Meteorology. Elsevier Academic, 535 pp.
- Houze, R. A., and Coauthors, **2006**: The Hurricane Rainband and Intensity Change Experiment: Observations and modeling of Hurricanes Katrina, Ophelia, and Rita. *Bull. Amer. Meteor. Soc.*, 87, 1503–1521.
- Houze, R. A., S. S. Chen, B. F. Smull, W.-C. Lee, and M. M. Bell, **2007**: Hurricane intensity and eyewall replacement. *Science*, 315, 1235–1239.
- Huang, Y.-H., Montgomery, M. T. and Wu, C.-C., **2012**: Concentric eyewall formation in Typhoon Sinlaku (2008). Part II: Axisymmetric dynamical processes. *J. Atmos. Sci.*, 69, 662-674.
- Judt, F., and S. S. Chen, **2010**: Convectively generated potential vorticity in rainbands and formation of the secondary eyewall in Hurricane Rita of 2005. *J. Atmos. Sci.*, 67, 3581–3599.
- Kepert, J. D., **2013**: How Does the Boundary Layer Contribute to Eyewall Replacement Cycles in Axisymmetric Tropical Cyclones? *J. Atmos. Sci.*, 70, 2808-2830.
- Kepert, J. D. and D. S. Nolan, **2014**: Reply. *J. Atmos. Sci.*, in press.
- Kieu, C. Q., **2012**: An investigation into the contraction of the hurricane radius of maximum wind. *Meteorol. Atmos. Phys.*, 115, 47-56.
- Kimball, S. K. and M. S. Mulekar, **2004**: A 15-Year Climatology of North Atlantic Tropical Cyclones. Part I: Size Parameters. *J. Climate*, 17, 3555-3575.

- Klein, P. M., P. A. Harr, and R. L. Elsberry, **2000**: Extratropical transition of western North Pacific tropical cyclones: An overview and conceptual model of the transformation stage. *Wea. Forecasting*, 15, 373–395.
- Knaff, J. A., S. P. Longmore, D. A. Molenaar, **2014**: An Objective Satellite-Based Tropical Cyclone Size Climatology. *J. Climate*, 27, 455–476.
- Knapp, K. R., **2008**: Hurricane satellite (HURSAT) data sets: Low Earth orbit infrared and microwave data. Preprints, 28th Conf. on Hurricanes and Tropical Meteorology, Orlando, FL, Amer. Meteor. Soc., 4B.4.
- Kossin, J. P., and M. Sitkowski, **2009**: An objective model for identifying secondary eyewall formation in hurricanes. *Mon. Wea. Rev.*, 137, 876–892.
- Kuo, H.-C., C.-P. Chang, Y.-T. Yang, and H.-J. Jiang, **2009**: Western North Pacific typhoons with concentric eyewalls. *Mon. Wea. Rev.*, 137, 3758–3770.
- Kuo, H.-C., C.-P. Chang, and C.-H. Liu, **2012**: Convection and rapid filamentation in Typhoon Sinlaku during TCS-08/ T-PARC. *Mon. Wea. Rev.*, 140, 2806–2817.
- Liu, K. S. and J. C. L. Chan, **2002**: Synoptic flow patterns associated with small and large tropical cyclones over the western North Pacific. *Mon. Wea. Rev.*, 130, 2134–2142.
- Maclay, K. S., M. DeMaria, and T. H. V. Haar, **2008**: Tropical cyclone inner-core kinetic energy evolution. *Mon. Wea. Rev.*, 136, 4882–4898.
- Martinez, Y., G. Brunet, and M. K. Yau, **2010**: On the dynamics of two-dimensional hurricane-like concentric rings vortex formation. *J. Atmos. Sci.*, 67, 3253–3268.
- Menelaou, K., M. K. Yau, and Y. Martinez, **2012**: On the dynamics of the secondary eyewall genesis in Hurricane Wilma (2005). *Geophys. Res. Lett.*, 39, L04801, doi:10.1029/2011GL050699.
- Merrill, R. T., **1984**: A comparison of large and small tropical cyclones. *Mon. Wea. Rev.*, 112, 1408–1418.
- Mohapatra, M. and Monica S., **2014** (communicated to *Int. J. of Remote Sensing*)
- Moon, Y., and D. S. Nolan, **2014a**: Spiral rainbands in a numerical simulation of Hurricane Bill (2009). Part I: Structures and comparisons to observations. *J. Atmos. Sci.*, in press.
- Moon, Y., and D. S. Nolan, **2014b**: Spiral rainbands in a numerical simulation of Hurricane Bill (2009). Part II: Propagation of inner rainbands. *J. Atmos. Sci.*, in press.
- Montgomery, M. T., and R. J. Kallenbach, **1997**: A theory for vortex Rossby waves and its application to spiral bands and intensity changes in hurricanes. *Quart. J. Roy. Meteor. Soc.*, 123, 435–465.
- Montgomery, M. T., S. F. Abarca, R. K. Smith, C. C. Wu and Y. H. Huang, **2014**: Comments on “How does the boundary layer contribute to eyewall replacement cycles in axisymmetric tropical cyclones?” by J. D. Kepert. Accepted. *J. Atmos. Sci.*
- Moyer, A. C., J. L. Evans, and M. Powell, **2007**: Comparison of observed gale radius statistics. *Meteor. Atmos. Phys.*, 97, 41–55.
- Murray, D.A., **2009**: Improved Short-Term Atlantic Hurricane Intensity Forecasts Using Reconnaissance-based Core Measurements. M.S. Thesis, Florida State University, 150 pp.
- Musgrave, K. D., **2011**: Tropical cyclone inner core structure and intensity change. PhD Dissertation, Colo. State Univ., 103 pp.
- Musgrave, K. D., R. K. Taft, J. L. Vigh, B. D. McNoldy, W. H. Schubert, **2012**: Time evolution of the intensity and size of tropical cyclones. *Journal of Advances in Modeling Earth Systems*, 4, M08001.

- Nolan, D. S., R. E. Hart, J. F. Price, G. M. Barnes, M. T. Montgomery, and J. Goerrs, **2013**: 1ST Report of the Scientific Review Committee (SRC) for the Hurricane Forecast Improvement Project (HFIP).
- Pan, C. J., K. K. Reddy, H. C. Lai, **2010**: Wind profiler observations on orographic effects of typhoon wind structure modification over Taiwan (120.38°E, 22.6°N). *Ann. Geophys.*, **28**, 141–147.
- Piech, D., **2007**: Atlantic Reconnaissance Vortex Message Climatology and Composites and Their Use in Characterizing Eyewall Cycles. M.S. Thesis, Florida State Univ., 139 pp.
- Poe, G.A.; **1990**, "Optimum interpolation of imaging microwave radiometer data," *Geoscience and Remote Sensing, IEEE Transactions on* , vol.28, no.5, pp.800-810.
- Powell, M. D., **1990a**: Boundary layer structure and dynamics in outer hurricane rainbands. Part I: Mesoscale rainfall and kinematic structure. *Mon. Wea. Rev.*, **118**, 891-917.
- Powell, M. D., **1990b**: Boundary layer structure and dynamics in outer hurricane rainbands. Part II: Downdraft modification and mixed-layer recovery. *Mon. Wea. Rev.*, **118**, 918-938.
- Qiu, X., and Tan, Z.-M., **2012**: The roles of asymmetric inflow forcing induced by outer rainbands in tropical cyclone secondary eyewall formation. *J. Atmos. Sci.*, **70**, 953-974.
- Quinting, J. F., M. M. Bell, P. A. Harr, and S. C. Jones, **2014**: Structural characteristics of T-PARC Typhoon Sinlaku during its extratropical transition. *Mon. Wea. Rev.*, **142**, 1945-1961.
- Raghavan, S., **1997**, "Radar observations of tropical cyclones over the Indian seas", *Mausam*, **48**, 169-188.
- Reasor, P. D., R. Rogers, and S. Lorsolo, **2013**: Environmental flow impacts on tropical cyclone structure diagnosed from airborne Doppler radar composites. *Mon. Wea. Rev.*, **141**, 2949–2969,
- Reasor, P.D., Eastin, M.D. and J.F. Gamache, **2009**: Rapidly intensifying Hurricane Guillermo (1997). Part I: Low-wavenumber structure and evolution, *Mon. Wea. Rev.*, **133**, 209-227.
- Riemer, M., M. T. Montgomery, and M. E. Nicholls, **2010**: A new paradigm for intensity modification of tropical cyclones: Thermodynamic impact of vertical wind shear on the inflow layer. *Atmospheric Chemistry and Physics*, **10**, 3163–3188.
- Riemer, M., M. T. Montgomery, and M. E. Nicholls, **2013**: Further examination of the thermodynamic modification of the inflow layer of tropical cyclones by vertical wind shear. *Atmos. Chem. Phys.*, **13**, 327–346,
- Rogers, R.F., Reasor, P. and S. Lorsolo, **2013**: Airborne Doppler observations of the inner-core structural differences between intensifying and steady-state tropical cyclones. *Mon. Wea. Rev.*, **141**, 2970-2991.
- Rotunno, R. and G. H. Bryan, **2012**: Effects of Parameterized Diffusion on Simulated Hurricanes. *J. Atmos. Sci.*, **69**, 2284–2299.
- Rozoff, C. M., D. S. Nolan, J. P. Kossin, F. Zhang, and J. Fang, **2012**: The roles of an expanding wind field and inertial stability in tropical cyclone secondary eyewall formation. *J. Atmos. Sci.*, **69**, 2621–2643.
- Sampson, C. R., A. J. Schrader, **2000**: The Automated Tropical Cyclone Forecasting System (Version 3.2). *Bull. Amer. Meteor. Soc.*, **81**, 1231–1240.
- Sanabia, E. R., **2010**: The re-intensification of Typhoon Sinlaku (2008). Ph.D. thesis, Naval Postgraduate School, Monterey, CA, 213 pp. [Available online at http://edocs.nps.edu/npspubs/scholarly/dissert/2010/Jun/10Jun_Sanabia_PhD.pdf.]
- Sawada, M., T. Iwasaki, **2010**: Impacts of Evaporation from Raindrops on Tropical Cyclones. Part I: Evolution and Axisymmetric Structure. *J. Atmos. Sci.*, **67**, 71–83.
doi: <http://dx.doi.org/10.1175/2009JAS3040.1>

- Sawada, M., T. Iwasaki, **2010**: Impacts of Evaporation from Raindrops on Tropical Cyclones. Part II: Features of Rainbands and Asymmetric Structure. *J. Atmos. Sci.*, 67, 84–96.
doi: <http://dx.doi.org/10.1175/2009JAS3195.1>
- Shapiro, L. J. and H. Willoughby, **1982**: The response of balanced hurricanes to local sources of heat and momentum. *J. Atmos. Sci.*, 39, 378–394.
- Shu, H., L. Ying, X. Ying-long, **2012**: A statistical analysis on intensity and structure changes of tropical cyclones making landfall on Taiwan island. *Journal of Tropical meteorology* (in Chinese) 28(3): 300-310.
- Shu, H., L. Ying, W. Na, **2013**: Diagnostic analysis on Nari (0116) structure and intensity changes during its landfall process on Taiwan Island. *Chinese Journal of Atmospheric Sciences* (in Chinese), 37 (1): 81-90.
- Sitkowski, M., J. P. Kossin, and C. M. Rozoff, **2011**: Intensity and structure changes during hurricane eyewall replacement cycles. *Mon. Wea. Rev.*, 139, 3829-3847.
- Smith, R. K., Montgomery, M. T. and Nguyen, S. V., **2009**: Tropical cyclone spin-up revisited. *Q. J. R. Meteorol. Soc.*, 135, 1321–1335.
- Smith, R. K., **2006**: Accurate determination of a balanced axisymmetric vortex. *Tellus*, 58, 98–103, doi:10.1111/j.1600-0870.2006.00149.x.
- Stern, D.P. and D.S. Nolan, **2009**: Reexamining the vertical structure of tangential winds in tropical cyclones: observations and theory. *J. Atmos. Sci.*, 66, 3579-3600.
- Stern, D. P., Brisbois, J.R. and D.S. Nolan, **2014**: An expanded dataset of hurricane eyewall sizes and slopes. *Mon. Wea. Rev.*, 71, 2747-2762.
- Stern, D. P., and D. S. Nolan, **2011**: On the vertical decay rate of the maximum tangential winds in tropical cyclones. *J. Atmos. Sci.*, 68, 2073–2094.
- Stern, D. P., and D. S. Nolan, **2012**: On the height of the warm core in tropical cyclones. *J. Atmos. Sci.*, 69, 1657–1680.
- Stern, D. P., and F. Zhang, **2013**: How does the eye warm? Part I: A potential temperature budget analysis of an idealized tropical cyclone. *J. Atmos. Sci.*, 70, 73–90.
- Stern, D. P., and F. Zhang, **2013b**: How does the eye warm? Part II: Sensitivity to vertical wind shear and a trajectory analysis. *J. Atmos. Sci.*, 70, 1849–1873.
- Stovern, D. R. and E. A. Ritchie, **2012**: The Importance of Atmospheric Temperature on the Size and Structure of Tropical Cyclones, Proceedings of the AMS 30th Conference on Hurricanes and Tropical Meteorology, 15-20 May 2012, Ponte Vedra Beach, FL.
- Stovern, D. R. and E. A. Ritchie, **2014**: Sensitivity of tropical cyclone size and structure changes to the environmental temperature, Part 1: Impacts of changing the initial temperature profile. (*To be submitted to J. Atmos. Sci.*).
- Stovern D. R. and E. A. Ritchie, **2014**: Sensitivity of tropical cyclone size and structure changes to the environmental temperature, Part 2: Importance of air-sea temperature difference. (*To be submitted to J. Atmos. Sci.*).
- Sun, Y. Q., Jiang, Y., Tan, B. and Zhang, F., **2013**: The governing dynamics of the secondary eyewall formation of Typhoon Sinlaku (2008). *J. Atmos. Sci.*, 70, 3818-3837.
- Terwey, W., S. F. Abarca, M. T. Montgomery, **2013**: Comments on “Convectively Generated Potential Vorticity in Rainbands and Formation of the Secondary Eyewall in Hurricane Rita of 2005.” *J. Atmos. Sci.*, 70, 984–988.
- Vigh, J. L., **2010**: Formation of the hurricane eye. Ph.D. dissertation, Colorado State University, 538 pp.
- Vigh, J. L., J. A. Knaff, W. H. Schubert, **2012**: A Climatology of Hurricane Eye Formation. *Mon. Wea. Rev.*, 140, 1405–1426.

- Wang, H., and Y. Wang, **2014**: A numerical study of Typhoon Megi (2010). Part I: Rapid intensification. *Mon. Wea. Rev.*, 142, 29–48.
- Wang, Y., **2002**: Vortex Rossby waves in a numerically simulated tropical cyclone. Part II: The role in tropical cyclone structure and intensity changes. *J. Atmos. Sci.*, 59, 1239-1262.
- Wang, Y., **2009**: How do outer spiral rainbands affect tropical cyclone structure and intensity? *J. Atmos. Sci.*, 66, 1250–1273.
- Wang, Y., **2012**: Recent Research Progress on Tropical Cyclone Structure and Intensity, Tropical Cyclone Research and Review, Volume 1, No. 2, pp.254-275.
- Wang, X., Ma, Y. and Davidson, N. E., **2013**: Secondary eyewall formation and eyewall replacement cycles in a simulated hurricane: effect of the net radial force in the hurricane boundary layer. *J. Atmos. Sci.*, 70, 1317-1341.
- Weatherford, C. L., W. M. Gray, **1988a**: Typhoon Structure as Revealed by Aircraft Reconnaissance. Part I: Data Analysis and Climatology. *Mon. Wea. Rev.*, 116, 1032–1043.
- Weatherford, C. L., W. M. Gray, **1988b**: Typhoon Structure as Revealed by Aircraft Reconnaissance. Part II: Structural Variability. *Mon. Wea. Rev.*, 116, 1044–1056.
- Williams, G. J., R. K. Taft, B. D. McNoldy and W. H. Schubert, **2014**: Shock-like structures in the tropical cyclone boundary layer. *JAMES*. 10.1002/jame.20028
- Willoughby, H. E., J. A. Clos, and M. G. Shoreibah, **1982**: Concentric eyewalls, secondary wind maximum, and the evolution of the hurricane vortex. *J. Atmos. Sci.*, 39, 395-411
- Wimmers, A. J., C. S. Velden, **2010**: Objectively Determining the Rotational Center of Tropical Cyclones in Passive Microwave Satellite Imagery. *J. Appl. Meteor. Climatol.*, 49, 2013–2034.
- Wu, C.-C., Huang, Y.-H. and Lien, G.-Y., **2012**: Concentric eyewall formation in Typhoon Sinlaku (2008). Part I: Assimilation of T-PARC data based on the ensemble Kalman filter (EnKF). *Mon. Wea. Rev.*, 140, 506-527.
- Xu, J. and Y. Wang, **2010a**: Sensitivity of tropical cyclone inner-core size and intensity to the radial distribution of surface entropy flux. *J. Atmos. Sci.*, 67, 1831-1852.
- Xu, J. and Y. Wang, **2010b**: Sensitivity of the simulated tropical cyclone inner-core size to the initial vortex size. *Mon. Wea. Rev.*, 138, 4135-4157.
- Yang, S., J. Hawkins, and K. Richardson, **2014**: The Improved NRL Tropical Cyclone Monitoring System with a Unified Microwave Brightness Temperature Recalibration Scheme. *Remote Sensing*, in revision.
- Ying, Y. and Zhang, Q., **2012**: A modeling study on tropical cyclone structure changes in response to ambient moisture variations. *J. Met. Soc. of Japan*, Vol. 90, No. 5, pp. 755-770.
- Yu, C.-K., Y. Chen, **2011**: Surface Fluctuations Associated with Tropical Cyclone Rainbands *Observed. Ann, Geophys.*, 28,141-147,2010
- Zhang, J. A. and M.T. Montgomery, **2012**: Observational Estimates of the Horizontal Eddy Diffusivity and Mixing Length in the Low-Level Region of Intense Hurricanes. *J. Atmos. Sci.*, 69, 1306–1316.
- Zhou, X., and B. Wang, **2011**: Impact of secondary eyewall heating on tropical cyclone intensity change. *J. Atmos. Sci.*, 68, 450-456.
- Zhu, Z., and P. Zhu, **2014**: The role of outer rainband convection in governing eyewall replacement cycle in numerical simulations of tropical cyclones. *J. of Geophysical Res.* 10.1002/2014JD021899.7